REPORT DOCUMENTATION PAGE

1a. REPORT SECURITY CLASSIFICATION UNCLASSIFIED	1b. RESTRICTIVE MARKINGS
2a. SECURITY CLASSIFICATION AUTHORITY	3. DISTRIBUTION / AVAILABILITY OF REPORT Approved for public release; distribution unlimited.
2b. DECLASSIFICATION / DOWNGRADING SCHEDULE	
4. PERFORMING ORGANIZATION REPORT NUMBER(S) TR 7635	5. MONITORING ORGANIZATION REPORT NUMBER(S)
6a. NAME OF PERFORMING ORGANIZATION Naval Underwater Systems Center 6b. OFFICE SYMBOL (*If applicable*)	7a. NAME OF MONITORING ORGANIZATION
6c. ADDRESS (*City, State, and ZIP Code*) New London Laboratory New London, Connecticut 06320	7b. ADDRESS (*City, State, and ZIP Code*)
8a. NAME OF FUNDING / SPONSORING ORGANIZATION Naval Oceanographic Research and Development Activity 8b. OFFICE SYMBOL (*If applicable*) Code 113	9. PROCUREMENT INSTRUMENT IDENTIFICATION NUMBER
8c. ADDRESS (*City, State, and ZIP Code*)	10. SOURCE OF FUNDING NUMBERS PROGRAM ELEMENT NO. 62759 / PROJECT NO. A67001 / TASK NO. / WORK UNIT ACCESSION NO.

11. TITLE (*Include Security Classification*)
ACOUSTIC SCATTERING FROM COMPOSITE WIND-WAVE SURFACES II: BACKSCATTER CROSS SECTIONS AND DOPPLER EFFECTS AT HIGH FREQUENCIES AND SMALL ANGLES FOR "BUBBLE-FREE" REGIMES

12. PERSONAL AUTHOR(S)
David Middleton

13a. TYPE OF REPORT	13b. TIME COVERED FROM _____ TO _____	14. DATE OF REPORT (*Year, Month, Day*)	15. PAGE COUNT
		1986, July 22	69

16. SUPPLEMENTARY NOTATION

17. COSATI CODES			18. SUBJECT TERMS (*Continue on reverse if necessary and identify by block number*)
FIELD	GROUP	SUB-GROUP	Bubble-free, high-frequency scatter Comparisons between experiment and theory Doppler shift

19. ABSTRACT (*Continue on reverse if necessary and identify by block number*)

The calculation of underwater acoustic backscatter cross sections for truly composite wind-wave surface is extended and improved over that of an initial investigation [1]. The improvement is provided by a new model of the postulated surface soliton ensemble which acts as the dominant scatter mechanism at high frequencies O(5-25 kHz), small grazing angles O(10°) here, and near-surface environments which are effectively "bubble-free," as demonstrated by the recent experiments of Roderick et al. [2].

In addition, with the new model, doppler shift δf_0 and doppler spread ΔF are defined with results in close agreement with empirical data [2]. From these, in turn, the pertinent parametric values of the soliton ensemble, namely, intensity level σ_ξ^2, surface speed c_s, and rms "wavelength" σ_h are obtained for the experiments in question [2]. The form, as well as the measure, of the results, agrees well with the theoretical predictions.

20. DISTRIBUTION / AVAILABILITY OF ABSTRACT	21. ABSTRACT SECURITY CLASSIFICATION
☐ UNCLASSIFIED/UNLIMITED ☒ SAME AS RPT. ☐ DTIC USERS	UNCLASSIFIED
22a. NAME OF RESPONSIBLE INDIVIDUAL William I. Roderick	22b. TELEPHONE (*Include Area Code*) (203)440-4305 / 22c. OFFICE SYMBOL Code 33A3

18. (Cont'd)

Doppler spread
Drift current speed, layer
Scattering cross sections
Small grazing angles
Soliton scattering mechanisms
Surface soliton ensemble
Underwater acoustic scattering

19. (Cont'd)

The nondispersive character of the soliton scattering surface component is clearly demonstrated in the doppler shift observations, where noticeable surface drift velocities must be included (in addition to a measured deep current). On the other hand, doppler shifts based on the classical dispersive wave model agree poorly with experiment, especially when surface drift speeds are included.

The doppler spread is produced by three modulation mechanisms: (1) random phase modulation (of the scattered signal) generated by the movement of the large-scale (gravity-capillary) surface component; (2) a random phase modulation associated with the variability of the surface drift and current speeds; and (3) a random amplitude modulation (AM) stemming from the local "tilting" of the large-scale component, on which the thin drift current and soliton ensemble ride, in turn. While these phase modulations are proportional to the illuminating frequency (f_o), the amplitude modulation, which is particularly evident at the lower frequencies O(15-5 kHz), is frequency-independent. Failure to account for these AM effects destroys agreement between theory and experiment. (For example, including the AM contributions gives a much too large result O(45 Hz at f_o = 20 kHz) for ΔF when the classical result is used, cf. Sec. 10).

The report is divided into two parts: Part I gives a presentation of the problem, with a detailed summary, comparison, and discussion of the theoretical and experimental results. It is shown that the various general "classical" models cannot account satisfactorily for the observations as a whole, whereas the present model, although not yet conclusively established, does so very well. Part II provides the analysis from which the results of Part I are obtained.

NUSC Technical Report 7635
22 July 1986

Acoustic Scattering from Composite Wind-Wave Surfaces II: Backscatter Cross Sections and Doppler Effects at High Frequencies and Small Angles for "Bubble-Free" Régimes

David Middleton
(Consultant)

Surface Ship Sonar Department

Naval Underwater Systems Center
Newport, Rhode Island / New London, Connecticut

Preface

This work was accomplished under NUSC Project No. A67001, "High Frequency Acoustic Program," Principal Investigator, Dr. W. I. Roderick (Code 33A3). The sponsoring activity is Naval Oceanographic Research and Development Activity (NORDA), Program Manager, Dr. R. Farwell, Code 113. Funding is provided under Program Element 62759. This report was prepared for Dr. Roderick (Code 33A3, NUSC) by Dr. David Middleton, 127 E. 91 St., New York, NY 10128, under Contract Nos. N00140-84-M-MS42 and N00140-84-M-NM82.

The Technical Reviewer for this report was Dr. Roderick (Code 33A3).

The author again wishes, in particular, to thank Dr. Roderick for his interest in, and critique of this research, and for the many stimulating discussions regarding the author's scatter model and results.

Reviewed and Approved: 22 July 1986

L. Freeman
Head, Surface Ship Sonar Department

The Principal Investigator of this report is located at the New London Laboratory, Naval Underwater Systems Center, New London, Connecticut 06320.

Table of Contents

List of Figures

List of Principal Symbols

A_1 = effective scattering area, (6.3), (6.6a)

A_o = signal amplitude

$\underset{\sim}{\alpha}_o$ = directional wave vector

$\underset{\sim}{\alpha}_{o\perp}$ = directional vector in (x,y)-plane

α = angle of wave movement

C = wave spectrum constant, (1.1)

$\hat{C}$ = doppler spread width parameter, Eq. (10.10)

c_s = soliton speed

c_o = (av.) speed of sound in water

δ = delta function

δf_o = mean doppler shift

$\delta\omega_o$ = $2\pi\delta f_o$

F_2, $F_{2\text{-}G}$ = characteristic functions

ΔF = (rms) doppler spread

f_1, f_s, f_o = frequencies

$G^{(1)}$ = scale constant (6.2a)

g = 9.80 m/sec^2

g_T, g_R = beam gains

h_{eff} = effective soliton channel depth

$\hat{\underset{\sim}{i}}_x$, $\hat{\underset{\sim}{i}}_y$, $\hat{\underset{\sim}{i}}_z$ = unit vectors

$\hat{\underset{\sim}{i}}_c$, $\hat{\underset{\sim}{i}}_S$, $\hat{\underset{\sim}{i}}_d$ = unit vectors (7.4)

K_1 = modified Bessel function of second kind, Eq. (9.7)

K_S, $K_{N(0)}$, K_{in} = covariances

k, k_o = wave numbers

L_o = soliton wavelength

λ, λ_o = wavelengths

$M_{RT}^{(0)}$ = a covariance, cf. (6.3)

$N_{SG}^{(0)}$ = "tilt" factor

ν, $\underset{\sim}{\nu}$, $\underset{\sim}{\nu}_o$ = wave numbers

$\underset{\sim}{\hat{n}}$ = unit normal

$O(\ )$ ≡ the Bachmann-Landau symbol meaning "of the order of"

ω, ω_s, ω_o = angular frequencies

Φ_w = mean wind direction

ϕ_{oT} = azimuthal angle, Fig. 2.1

$\underset{\sim}{\Delta r}$, Δr = spatial difference

$\overline{R_o^2}$ = mean square (plane wave) reflection coefficient

R_G = amplitude modulation parameter (doppler spread)

ρ_G = normalized covariance

$\overline{S^2}$ = mean square shadowing function

σ_G^2 = $\overline{\zeta_G^2}$, (8.5)

$\hat{\sigma}_s^{(0)}$, $\hat{\sigma}_g^{(0)}$, $\hat{\sigma}_c$, $\hat{\sigma}_{(inc)}^{(0)}$ = (incoherent) backscatter cross sections

σ_ζ^2, $\sigma_{\dot{\zeta}}^2$, σ_S^2, σ_h^2 = dimensional (length, height, etc.) variances

σ_{Gx}, σ_x = rms slopes

σ_β = rms doppler spread, Eq. (8.4)

θ_{oT} = polar angle (Fig. 1.1)

τ = t_2-t_1

U_a, $\overline{U_a}$ = near-surface wind velocities

$\underset{\sim}{v}_D$, v_{oD}, $\overline{v}_{oD}$, v_d = wave and fluid speeds and velocities

W = frequency spectrum

W = wave number spectrum

ζ, $\zeta(r,t)$ = wave height

ζ_x, ζ_y = surface slopes

Acoustic Scattering from Composite Wind-Wave Surfaces II: Backscatter Cross Sections and Doppler Effects at High Frequencies and Small Angles for "Bubble-Free" Régimes†*

by
David Middleton**
(August, 1985)

1. Introduction

The present study continues the investigation of the author embodied in NUSC Technical Document TD-7205, [1]. Here we are again concerned with underwater acoustic scattering from the random moving wind-wave surface of the ocean. In particular, we are concerned with high frequency O(5-20 kHz), small grazing angle configurations O(5-25°), and near-surface as well as volume régimes which are bubble-free vis-à-vis surface effects [1], [2].. Our efforts here are specifically directed to the calculation of doppler shift and doppler spread produced by the wind-driven ocean surface. Included also is a summary of a more complete model of the soliton scattering mechanism originally postulated and described in [1]. This more complete model is based on recent work of Middleton [3], [4] and Mellen [4]. It presents a much fuller account of the nonlinear wind-wave surface interactions, one of whose ultimate products is the surface-riding soliton ensemble which much empirical evidence suggests [3], [4] provides the effective scattering mechanism results observed in practice in "bubble-free" situations [2]. A number of new calculations of backscatter cross sections in comparison with experimental data are accordingly included here, cf. [3], [4] also, to reinforce the plausibility of our postulated surface scatter model, in conjunction with the doppler analysis, which is the main topic of this report.

---

†This is Part II, continuing the author's earlier study, "Acoustic Scattering Cross Sections for Truly Composite Wind-Wave Surfaces: Scattering Without Bubbles," NUSC Tech. Doc. 7205, August 20, 1984 (NUSC, New London, Conn. 06320).

*Work supported under contracts with the Naval Underwater Systems Center (NUSC), New London, Conn. 06320, Contracts N00140-84-M-MS42 and N00140-84-M-NM82.

**Contractor, Physics and Applied Mathematics, 127 E. 91 St., New York, NY 10128.

1.1 Background

As noted above (and in [1], [2], [5], [6], for example), it has been widely observed for both above-surface (electromagnetic-EM) scattering and underwater acoustic scattering from wind-wave ocean surfaces that such scattering is much more intense O(15-20 db) in the high frequency régime, distinguished by large Rayleigh numbers, with moderate to fairly strong mean surface winds, $\overline{U}_a$ = O(5-15 m/sec) than classical theoretical scattering models, even those based on composite surfaces composed of gravity and capillary components, can predict [1], [5], [6]. This phenomenon becomes evident at small grazing angles, where the short-wavelength components of the surface scatter dominate. It is especially noticeable in the acoustic cases, cf. Sec. 1 of [1]. For the EM cases, where X-band radar is employed, the recent results of de Loor [7] and Lawner and Moore [8] (Fig. 4 especially) are similarly noted.

In most underwater acoustic scattering situations it has been usually postulated that a near-surface bubble mechanism, produced by breaking waves, is responsible for the much larger observed scattering cross sections at small grazing angles ([9], in addition to [5], [6]). However, recent, very precise experiments by Roderick and his group at NUSC [2] have shown that these comparatively large acoustic (backscatter) cross sections can occur without an observable contiguous subsurface bubble layer, under otherwise comparable geometrical and physical conditions.

A possible surface mechanism which can account for these significantly larger scatter returns and doppler shifts and spreads [2], when bubble structures prove empirically ignorable, has been suggested in [1], [3], [4]. It likewise appears as a critical product in the generation of wind-wave surfaces, as described in [4], Sec. 2. The mechanism in question is the ensemble of solitons, or hydraulic bumps [10], [11], which in this model are produced in consequence of the nonlinear wind-wave interactions or mutual modulations, impinging on a thin wind-driven water surface layer. This latter is a thin O(centimeter) moving surface layer which is developed when a nonzero mean wind speed ($\overline{U}_a > 0$) is established, as the fetch of the surface becomes larger; see Shemdin [12]; also Ramamonjiariosa [25]. [Its effective thickness for soliton support appears to be much thinner O(millimeters), cf. Sec. 3 ff.] Accordingly, the scattering interface postulated here and in [1] consists of a single wave surface

(usually artificially divided into so-called "gravity" and "capillary" wave components), and a truly additional component, namely the soliton "ripples." These now ride upon the moving wind-driven surface portion, i.e., the drift layer, of the gravity-capillary wave surface, in our initial model here.

1.2 Various Physical Models

It has been shown in [1] that the various analytical methods and approximations used in earlier analyses for the (scalar) surface scatter problem are essentially valid here and differ little among themselves in quantitative results. The observed large discrepancies between theory and experiment, noted above, must therefore be attributable to the choice of physical model ([1], Sec. 1). Moreover, on the empirical side, it is observed at once that the radar data ([7], [8] and refs. therein) indicate that the level of the wave-number (intensity) spectrum of the sea surface in the regions (k = 5+ to 0.5 rad cm^{-1}) depends markedly on the near-surface wind conditions. This implies that not only $\overline{U}_a$, but var U_a and higher moments, of the turbulent atmosphere, become important for a proper description of the sea surface: observations made at these wavelengths will depend on the particular sea surface actually generated.

The interpretation of the above is readily made: evidently, these empirical spectra are <u>unsaturated</u>, i.e., are dependent on $\overline{U}_a$, var U_a, etc., at the shorter wavelengths. This effect is evident in Fig. 4 of [8], in Fig. 11 of Mitsuyasu and Honda [13], where wave gauges rather than radar were employed; see also the remarks in the more recent paper [14]. A common example of a classical phenomenological spectrum which is saturated at the higher frequencies ($\sim\omega_s$) is that of Pierson and Moskowitz [15]:

$$W_\zeta(f_s) = Cg^2\omega_s^{-5}e^{-0.74g^4/\omega_s^4\overline{U}_a^4} \quad ; \quad C = 8.10 \cdot 10^{-3} \text{ (indep. of } \overline{U}_a, \text{ etc.)};$$

$$\omega_s = 2\pi f_s \ (\geqslant 0); \quad \overline{U}_a > 0. \tag{1.1}$$

Clearly, this spectrum is saturated, namely, independent of wind statistics ($\overline{U}_a$, etc.) as ω_s becomes large, for the ultragravity frequencies on up.

The empirical data noted above ([8], [13], [14]), however, imply that $C \rightarrow C(\overline{U}_a, \text{var } \overline{U}_a, \ldots)$. In particular, the data ([7], [8], for example) typically indicate spectrum levels to be O(10-20 db) above the classical ($\sim k^{-4}$) average level, at small angles ($\phi = 20° \rightarrow 10°$) by extrapolation. Accordingly, this increased level, when employed in the classical theory, could possibly account for the larger observed backscatter cross sections.

However, an increased level alone cannot explain the observed doppler shifts and doppler spreads {cf. Figs. 13, 14 of [2] and Figs. 3.1, 4.1 following in the present study}. Nor can such wave surface models, which are essentially linear, account adequately for the wind-wave interactions which produce the wave surface. Thus, we propose here, as in our earlier work [1], an explanation alternative to that of simply raising the spectral level of the gravity-capillary wave surface at the higher frequencies. The explanation chosen is that there is an additional surface phenomenon, namely, the soliton ensemble, which rides upon the moving drift-layer portion of the usual gravity-capillary wave surface. This ensemble is large enough to account for the observed backscatter cross sections--both acoustic [1] and radar--whenever a near-surface bubble layer is ignorable, as in Roderick's experiments [2]. This latter state can occur under many near-surface wind conditions, for example, with large $\overline{U}_a$ but small var U_a, corresponding to a steady near-surface wind with comparatively little turbulence, etc.

The reasons for choosing the soliton alternative here are, concisely:

(i). The basic wind-wave interactions whereby wind energy is transferred to the wave surface are <u>nonlinear</u>, i.e., are air-water "modulation" processes, taking place primarily in the high-wave number region of the wave surface spectrum, cf. [3], [4], and through turbulence transferring energy downward to the smaller wave numbers.

(ii). Solitons are the result of nonlinear forces, here hydrodynamically balanced by dispersive forces, and <u>they propagate nondispersively</u>, at constant speeds. These solitons have the required "shallow channel," in the form of the thin drift layer, which is needed to support their generation and propagation. [See refs. [6a], [12], [13] of [4] for further details, and in particular [3] and [32].

(iii). Observed doppler results (Figs. 13, 14 of [2]), also Fig. 3.1 here, are consistent with the linear frequency shifts required by such nondispersive elements as these surface solitons. (See, in particular, Fig. 1 of [25]). Moreover, the observed doppler spreads [2] are likewise consistent with the soliton and drift layer mechanisms, as we shall show in Sections 3 and 4 ff., cf. Fig. 4.1.

(iv). Finally, the soliton model here can also account for the noticeably larger than conventionally expected backscatter cross sections, cf. Sec. 2, as we have already noted above. Moreover, surface solitons can be generated with long, intermediate, and short (spatial) durations, as Olson et al. [20] and others [11] have demonstrated, so that scattering contributions may be expected over wavenumbers $O(2\pi/25$ to $2\pi/0.5$ cm^{-1}) typically, in the observed "high-frequency" ranges.

In all the above, we emphasize that at this stage of our experimental and theoretical knowledge the concept of the surface soliton ensemble as the dominant surface scatter mechanism at high frequencies and small grazing angles appears strongly plausible, but has not (yet) been proved. We regard it as a working hypothesis, consistent with a broad spectrum of physical evidence [2], [3], [4], [25], [32].

1.3 New Features of the Present Study

Accordingly, the new features of this present investigation are, concisely:

(1). A new evaluation of the underwater acoustic backscatter cross section, $\hat{\sigma}^{(0)}_{inc}$, now as a function of frequency O(5-20 kHz), for small grazing angles (9°), using the author's more complete model of the surface-soliton ensemble (cf. Secs. 2 and 9, ff.);

(2). Calculation of the doppler shift δf_o, produced by the combined effects of a deep current, the superficial wind-drift layer ([12], and [3], [4]), and the soliton movements on this layer (Secs. 3 and 7 ff.);

(3). A determination of doppler spread, ΔF, which is seen to consist primarily of spread due to that in the surface drift velocity and the motion of the primary ocean surface (gravity-capillary surface)

and includes the amplitude modulation effects of the latter on the small scale components (Secs. 4 and 10 ff.);

(4). A comparison of the above (1)-(3) with recent experimental data [2], Figs. 2.2, 3.1, 4.1; and

(5). A comparison of the present theoretical model with "classical" results based solely on the gravity-capillary wave surface, cf. Figs. 2.2, 3.1, 4.1, and text.

The principal results are presented and discussed in Part I, while the analytical derivations are reserved to Part II, as before [1].

1.4 Organization of the Report

The Report is organized as follows: Section 2 summarizes our recent results for the (underwater) acoustic backscatter cross section $\hat{\sigma}^{(0)}_{inc}$ as a function of frequency, at small grazing angles, based on the aforementioned surface soliton model, which is briefly summarized here and in Sec. 7 ff. Comparisons are made with Roderick et al.'s recent data [2] for bubble-free régimes and Golubin's earlier experiments [16], which represent different wind and surface environments. Section 3 considers the theory and measurements [2] of doppler shift, δf_o, while Section 4 treats analogous results for the associated doppler spread, ΔF. Section 5 completes the discussion of the joint theoretical and experimental results, which constitutes one of the two main endeavors of this study. The other is the analysis, provided in Secs. 6-10, Part II, which is based directly on the results of Part II, [1], to which the reader is referred for technical details.

Part I. Results and Discussion

2. Incoherent Backscatter Cross Sections

In the case of underwater acoustic backscatter, the incoherent backscatter cross section $\hat{\sigma}^{(0)}_{inc}$ consists of three main components:

$$\hat{\sigma}^{(0)}_{inc} = \left\{\hat{\sigma}^{(0)}_{g\text{-}inc} + \hat{\sigma}^{(0)}_{c\text{-}inc}\right\}_G + \hat{\sigma}^{(0)}_{S\text{-}inc}. \tag{2.1}$$

The first two stem from the gravity-capillary wave surface (G = g+c) and have been shown in [1] for the conditions of Roderick's experiments [2]

to be negligible compared with $\hat{\sigma}^{(0)}_{S\text{-inc}}$ at high signal frequencies ($f_o >$ 5 kHz) and small grazing angles ($\phi = 9°$). The third term represents the backscatter cross section associated with our postulated soliton ensemble moving on the wave surface (G). Here $\hat{\sigma}^{(0)}_{S\text{-inc}}$ is a Bragg scatter contribution similar to $\hat{\sigma}^{(0)}_{c\text{-inc}}$ and proportional now to the wave number intensity spectrum $W_2(\underset{\sim}{k}|0)_S$ of the surface-riding soliton ensemble. Specifically, we have

$$\boxed{\hat{\sigma}^{(0)}_{S\text{-inc}} = \overline{R_o^2}\ \overline{S^2}\ \frac{k_o^4}{16\pi^2}\ N^{(0)}_{GS\text{-inc}}\ W_2(\underset{\sim}{k}|0)_S,} \tag{2.2}$$

where

$\overline{R_o^2}$ = mean square reflection coefficient ($\doteq$ 1 here);

$\overline{S^2}$ = mean square shadowing function ($\doteq$ 1 here, also);

k_o = $2\pi/\lambda_o$; λ_o = wavelength of the (pulsed) cw (acoustic) excitation, in water;

$N^{(0)}_{GS\text{-inc}}$ = "tilt-factor," given by (7.66a) and Sec. 3.1A of [1]. (2.2a)

The soliton wave number spectrum $W_2(\underset{\sim}{k}|0)_S$ is found to be ([3], [4] and Sec. 8.4 ff.)

$$\boxed{W_2(\underset{\sim}{k}|0)_S = \frac{\pi\varepsilon_I\sigma_S^2\sigma_h^2}{[1 + (k\sigma_h/2)^2]^2}} \quad , k = 2k_o \sin\theta_{oT}, \tag{2.3}$$

with θ_{oT} the angle of the axis of the beam maximum with the vertical, so that $\phi(= \pi/2 - \theta_{oT})$ is the grazing angle. The backscatter geometry is sketched in Fig. 2.1. Here ε_I = 1 for semi-isotropic ($-\pi/2 < \phi < \pi/2$), = 2 for isotropic ($-\pi < \phi < \pi$) excitation [3] of the solitons on the wave surface. (The quantities σ_S^2, σ_h^2 are defined below in Eq. (2.6a).) From physical considerations we usually reject the isotropic model, since the soliton surface moves downwind.)

The tilt-factor $N^{(0)}_{GS}$ (= 16 $\hat{N}^{(0)}_{GS}$) accounts for the amplitude modulation

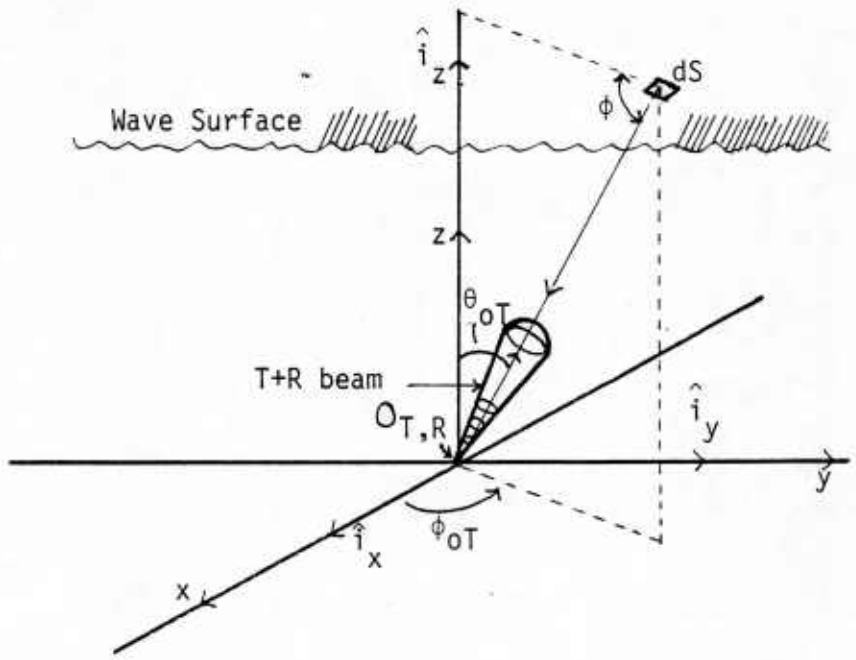

Figure 2.1 Backscatter Geometry

of the small-scale surface waves by the gravity wave component of the surface and is for these backscatter geometries:

$$N_{GS}^{(0)} \doteq 16\{3\sigma_{Gx}^2 \sin^4\theta_{oT} + 6\sigma_{Gx}^2 \sin^2\theta_{oT}\cos^2\theta_{oT} + \cos^4\theta_{oT}\}, \tag{2.4}$$

with $\phi_{oT} = \pi/2$; $\sigma_{Gx} = \sigma_{Gy}$.

Here the rms large-scale slopes are found numerically from Cox and Munk's result [17]

$$\sigma_{G(x=y)}^2 = \left.\overline{\left(\frac{\partial\zeta}{\partial x}\right)^2}\right|_G = (3.0 + 5.12\ \overline{U}_a)\cdot 10^{-3}. \tag{2.5}$$

The reflection coefficient is essentially unity here, and the shadowing coefficient is likewise, e.g., $\overline{S^2} \doteq 1$, as long as* $\theta_{oT} < 85°$ ($\phi > 5°$).

---

*For cases where $\overline{S^2} < 1$ and thus must be considered, see Bass and Fuks [18], Fig. 59, and recent work on underice scattering, Sec. 3.2C of [19].

Combining (2.4) and (2.3) in (2.2) gives the desired backscatter cross section explicitly (with $\varepsilon_I = 1$ now)

$$\hat{\sigma}_S^{(0)} = \frac{2}{\pi}\{3\sigma_{Gx}^4 \sin^4\theta_{oT} + 6\sigma_{Gx}^2 \sin^2\theta_{oT}\cos^2\theta_{oT} + \cos^4\theta_{oT}\}k_o^4 \frac{\sigma_S^2\sigma_h^2/2}{[1+(\sigma_h k_o \sin\theta_{oT})^2]^2}, \tag{2.6}$$

where

$$\begin{cases} \sigma_S^2 = \text{mean square intensity of the surface soliton ensemble (cf. Sec. 7.3);} \\ \sigma_h^2 = \overline{L_o^2} = \text{mean square "wave" length of the solitons.} \end{cases} \tag{2.6a}$$

Results of recent experiments and Eq. (2.6) of the present theory for acoustic backscatter are presented in Fig. 2.2, for $\theta_{oT} = 81°$ (or $\phi = 9°$) and $\hat{N}_{GS}^{(0)}$ ($= N_{GS}^{(0)}/16$) $= 1.68\ \ 10^{-2}$ for $\overline{U_a} = 10$ m/sec. Here $\overline{R_o^2} \doteq \overline{S^2} \doteq 1$ and +2.5 db has been added for the Kirchoff correction at these small grazing angles (all curves), cf. Table 3.1 and "footnote" thereto in [1]. The fit of theory to experiment is made for the above geometry over a range of 5-20 kHz. Narrow band signals, i.e., comparatively long cw pulses, are used in transmission and reception by Roderick et al., cf. Fig. 10 [2]. Explosive charges were employed by Galubin [16], also Fig. 1.26 of [9], with narrow-band reception. In Figure 2.2 the Φ represent the Roderick data [2], Fig. 10, while the $\otimes$-points are Galubin's data [16]. Included in Fig. 2.2 are some typical theoretical backscatter cross sections based on purely capillary resonance returns ([9], Sec. 9.11, Figs. 1.26, 9.10; and [1], Eq. (3.18)).

2.1 Discussion and Results

Clearly evident are the different near-surface wind states for the two data sets. Thus, although the mean wind speeds $\overline{U_a}$ were essentially the same (20 knots = 10 m/sec) in both instances, different wind states were in force, as quantified by different values of var U_a (and higher moments) although not recorded at the time. We infer this from the different thickness of the wind-drift layers ($\sim\sigma_h$) and hence average length of the surface solitons, and by the different rms soliton amplitudes ($\sim \sigma_S$). As Shemdin has shown ([12], Figs. 1 and 2), the greater the wind speed U_a (and $\therefore \overline{U_a}$), the faster moving but thinner is the resultant surface

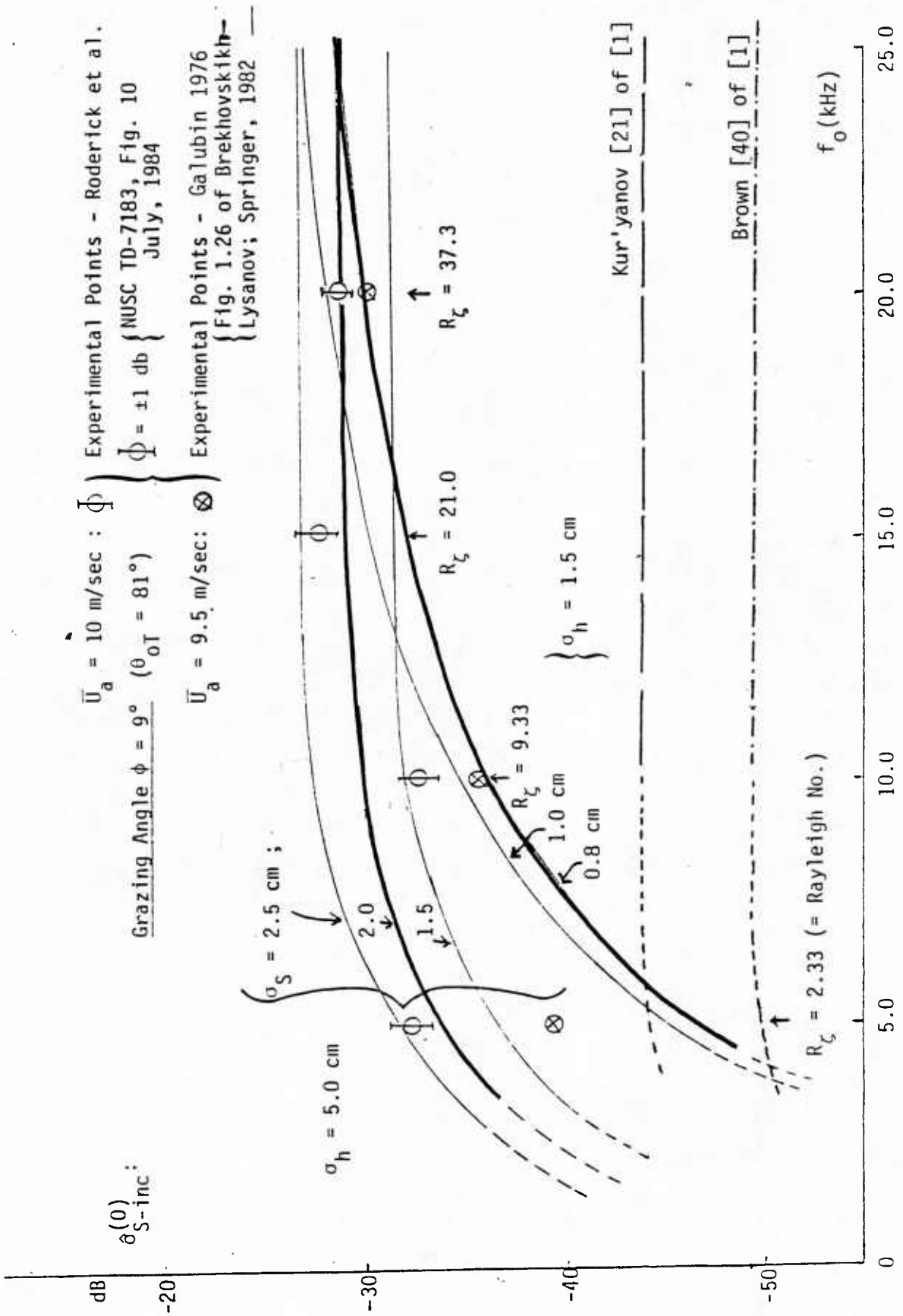

Figure 2.2 Incoherent Backscatter Cross Sections (Middleton Soliton Model, 1984-, [3], [4])

drift layer, and for fetches sufficiently large the drift layer velocity becomes nearly constant. This thinner layer can support larger and faster solitons, depending, of course, on the intensity and velocity of the initiating atmospheric shock waves [3], [4], [32].

Accordingly, on the basis of our postulated soliton model here we can deduce from Fig. 2.2 that the Roderick data are associated with a rather noticeable secular spread of wind speeds (~ large σ_h). To achieve the observed backscatter cross-sectional values, an appropriately larger soliton intensity (σ_S^2) is then required. With the present model this means that large but comparatively uniform shock wave intensities are maintained, leading to "large" soliton velocities (v_o) with small variances, at levels consistent with the data [2]. On the other hand, Galubin's data* imply a narrower spread (σ_h) in the drift layer, which suggests smaller var U_a. In addition, smaller values of v_o are needed, producing smaller levels of soliton intensity (σ_S^2) for nearly the same observed backscatter cross section at the higher frequencies.** From this we conclude that different near surface environmental states are represented by the two sets of data, even though $\overline{U_a}$ is effectively the same. This is consistent with our observation in Sec. 1.2, regarding the unsaturated wave spectra as frequency is increased.

In general, we also note that:

(i). Both the theoretical and empirical (incoherent) backscatter cross sections become independent of frequency as $k_o \to \infty$, cf. (2.6).

(ii). The potential existence of "long" solitons O(15-25 cm), as well as shorter ones, supports the possibility of backscatter returns at the lower "high" frequencies O(5 kHz), cf. Fig. 2.2, as well as at 20 kHz, etc. For examples of such solitons produced in tank experiments, see Figs. 2-6 of Olson et al. [20], esp. Fig. 2 where σ_h = 5.0 cm soliton length, $L_o \doteq$ 18 cm, and height σ_S ~ 3 cm, is typical of solitons capable of Bragg scatter at ~5 kHz.

---

*These are regarded as bubble-free here: Galubin's experimental procedure indicated negligible bubble effects in the volume but was not capable of discriminating a possible bubble surface layer.

**The noticeably larger value of $\hat{\sigma}_{xpt}^{(0)}$ at 5 kHz may be attributable to the growing contribution of the gravity-wave "facet" terms for these rather small Rayleigh numbers.

2.2 Remarks on the "Bubble-Free" State

Finally, a number of observations regarding the "bubble-fre" nature of Roderick's experiments [2] are in order:

(1). The resolution distance is $\tau_p c_o/2$, where τ_p = 0.4 msec is the pulse length used, directed normally to the wave surface from below, so that $\tau_p c_o/2$ = 0.30 m is the resolution distance here (cf. Fig. 3 of [2] and corrected text). Outside this distance about the mean surface elevation (ζ = 0) vis-à-vis the projector no bubbles distinguishable from the much lower volume reverberation were observed.

More precisely, operating at vertical incidence (θ_{oT} = 0) the receiving system was self-noise-limited such that if bubbles were present in the volume below the water/air surface, their backscattering strength would have to be more than -47 db to be apparent. This compares with -30 db actually observed for surface scatter ($\geq$ 15 kHz), cf. Fig. 2.2. No volume scatter at or above -47 db was noted as a precursor to the surface return, which indicates that the empirical backscatter returns in this experiment were well dominated by surface scattering mechanisms.

(2). Moreover, if near-surface bubbles are present in quantities sufficient to mask the surface and provide sufficient return to account for the observed levels, at these high frequencies and small grazing angles, the work of Glotov [21] and Thorpe [22] has shown that these bubbles will appear in variable layers O(2-4 meters) thick immediately below the surface. In particular, see Fig. 5D, p. 165 of [22]. This is much deeper than the 0.3 m resolution distance achieved by Roderick et al., cf. (1) above: no such layers were observed [2].

(3). When a masking bubble layer is present, there will be little or no observable doppler shift, neither for the now-masked resonant surface wave components nor any surface drift currents. The data of

[2], cf. Figs. 11, 13, show a very distinct and measureable doppler shift, in addition to an expected doppler broadening of the spectrum, Fig. 14, [2].

Thus, as we have noted above, and in [1], [3], [4], [32] the conclusion is drawn that some specific surface mechanism, here the proposed soliton ensemble (from the additional argument presented in Sec. 1.2), is responsible for the observed scatter results, when bubbles are ignorable. We emphasize that the surface soliton model advanced here, and in [1]-[4], [32], is so far inferentially supported by the data and physical argument, but has not yet been directly proved. A direct, quantitative demonstration of the soliton wave-surface component remains to be demonstrated explicitly, in the process of scattering. Nevertheless, as we show here, our soliton surface model is able to account for, and predict, not only cross-sectional values, but doppler shifts and spreads where the classical models fail, vide Table 5.1 ff.

3. The Mean Doppler Shift, δf_o: Theory and Experiment

From the analysis of Section 7, for the geometry of Fig. 7.1 which applies for the experiments of Roderick et al. [2], we have the (down) doppler shift (7.18a):

$$\delta f_o = -\frac{2\sin\theta_{oT}}{\lambda_o}\left\{c_S + \bar{v}_c \sin\phi_c + \bar{v}_d \sin\phi_w\right\}, \tag{3.1}$$

whose structure and derivation are discussed (7.18) ff.

The measured parameters of the model are [2]:

$$\begin{cases} \bar{v}_c = \text{(mean) deep current} = 26.0 \text{ cm/sec} & (3.2a) \\ \phi_c = \text{angle of current} = 51.5^\circ;\ \sin\phi_c = 0.783; & (3.2b) \\ \Phi_w = \text{mean wind direction} = 116^\circ;\ \sin\Phi_w = 0.899; & (3.2c) \\ \overline{U_a} = \text{mean (near surface) wind speed} = 10 \text{ m/sec}. & (3.2d) \end{cases}$$

In addition, the related backscatter geometry has

$$\phi_{oT} = \pi/2\ ; \quad \theta_{oT} = 81^\circ \quad (\phi = 9^\circ \text{ grazing angle}). \tag{3.3}$$

Furthermore, we assume that the surface drift layer moves in the mean wind direction (Φ_w), and that the measurements at f_o = 20 kHz are probably the most accurate. From the ensemble of measured δf_o's, represented by the points ⊗ in Fig. 3.1 (taken from Fig. 13 of [2]), we find that

$$(\delta f_o)_{expt.} = 12.4 \text{ Hz}, \quad (\lambda_o = 7.5 \text{ cm}), \tag{3.4}$$

and since

$$|\delta f_o| = \left(\frac{2\sin\theta_{oT}}{\lambda_o}\right)\overline{v_{oD}}; \quad \therefore \boxed{\left.\overline{v_{oD}}\right|_{xpt} = 47.0 \text{ cm/sec} = c_S + \overline{v_c}\sin\phi_c + \overline{v_d}\sin\Phi_w}, \tag{3.5}$$

where sin 81° = 0.988.

Our next step requires an assessment of $\overline{v_d}$. For this we consider a range of reasonable values, in part suggested by the "rule-of-thumb" that the mean drift speed is O(1-4%) of the mean wind speed $\overline{U_a}$ (Bass et al. [29]; [25], Fig. 5). Having specified a value of $\overline{v_d}$ we can then use (3.5) to obtain an estimate of the (total) soliton speed, $c_S = \hat{c}_o + v_o$, cf. Eq. 9.2 et seq. From the backscatter cross-sectional data of Fig. 2.2 we find that the rms soliton wavelength $\sigma_h = (\overline{L_o^2})^{\frac{1}{2}} = 5.0$ cm. From this and the estimate of c_S we then can show that the incremental soliton velocity v_o, due to the nonlinear mechanism involved [cf. Sec. 9] is ignorable vis-à-vis $c_S \doteq c_o$, and so deduce directly the effective thickness of the drift layer, h_{eff}, supporting the soliton mechanism.

We begin with the deep current and obtain

$$\overline{v_c}\sin 51.5° = 26 \sin 51.5° = 26(0.783) = 20.3 \text{ cm/sec}. \tag{3.6}$$

Table 3.1 shows values of c_S, h_{eff} and v_o, for a range of reasonable values of $\overline{v_d}$: the shaded portions of Table 3.1 appear to be appropriate to the model and circumstances described here. In addition, the relations used to determine c_S, h_{eff}, v_o, are (from Sec. 9 ff.)

$$c_S = \hat{c}_o + v_o = \sqrt{g h_{eff}} + v_o; \quad v_o = 4\, h_{eff}^{5/2}\, \sqrt{g}/3\overline{L_o^2}; \quad g = 980 \text{ cm/sec}^2, \tag{3.7}$$

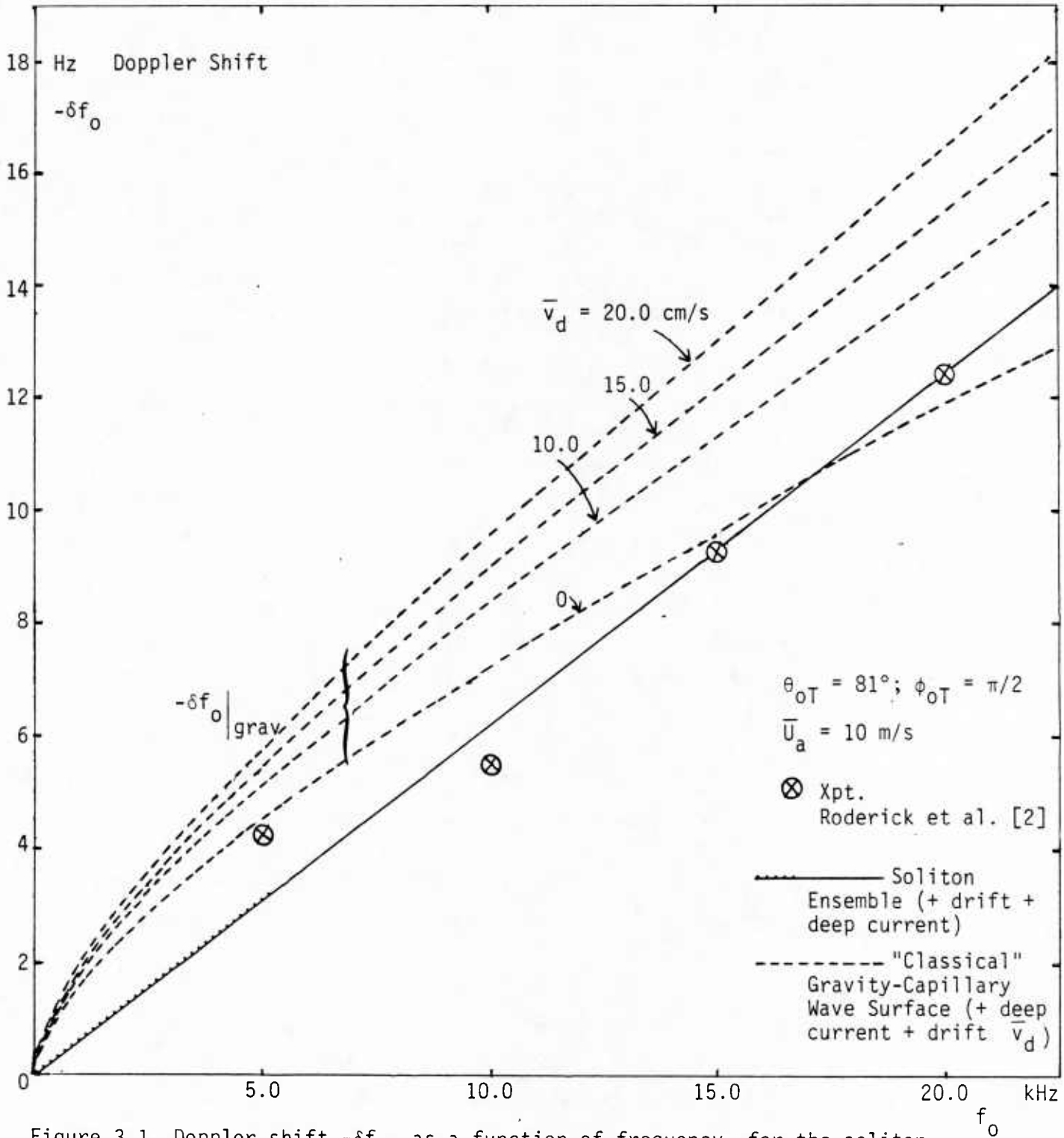

Figure 3.1 Doppler shift $-\delta f_o$, as a function of frequency, for the soliton (Eq. 13.1) and classical models (3.8), including surface drift and deep current speeds. Theory and experiment [2].

Table 3.1:

($\overline{U_a}$ = 10 m/sec)

$\overline{v_d}$	$\overline{v_d'}=\overline{v_d}\sin\Phi_w$	$c_S=\overline{v_{oD}}-20.3-\overline{v_d'}$	$h_{eff}\doteq c_s^2/g$	$h_{eff}^{5/2}$	v_o
10 cm/sec	**9.0 cm/sec**	**17.7 cm/sec**	**3.2 mm**	$5.79\cdot10^{-2}$	$9.7\cdot10^{-2}$ cm/sec
15.0	**13.5**	**13.2**	**1.8**	$1.37\cdot10^{-2}$	$2.3\cdot10^{-2}$
20.0	**18.0**	**8.7**	**0.77**	$1.6\cdot10^{-3}$	$2.7\cdot10^{-3}$
25.0	22.5	4.2	0.018	$4.3\cdot10^{-5}$	$7.2\cdot10^{-5}$
28.0	25.2	1.5	0.0023	$2.5\cdot10^{-7}$	$4.2\cdot10^{-7}$

and $v_o \ll c_o$ ($\doteq c_S$) here, with $L_o = 2L_{eff} = \sigma_h = 5.0$ cm [cf. Fig. 2.2 here] from the fit of the backscatter cross-sectional data of Roderick et al. [2]. Reasonable surface layer thicknesses and speeds of the surface soliton ensemble are noted in the shaded regions of Table 3.1, as well. [See, however, footnote, p. 50.]

If instead of the soliton surface model we employ the purely classical, linear model of a gravity-capillary wave surface, we find that in place of (3.1) the doppler shift δf_o is now given by (7.22b), namely,

$$\delta f_o\big|_{grav} = -\left\{\sqrt{\frac{g\sin\theta_{oT}}{\pi\lambda_o}} + \frac{2\sin\theta_{oT}}{\lambda_o}\left[\overline{v_c}\sin\phi_c + \overline{v_d}\sin\phi_w\right]\right\} \tag{3.8}$$

where $\lambda_o > 5$ cm, so that gravity waves predominate. Equation (3.8) includes the contributions of the observed deep current, and the surface drift. Figure 3.1 shows $\delta f_o\big|_{grav}$ for various mean drift speeds $0 \leqslant \overline{v_d} \leqslant 20$ cm/sec.

From the results above, namely (3.1) with (3.5) and Table 3.1, and (3.8), we see that the soliton surface model, which implies a linear doppler shift, fits the data well above 10 kHz and is not excessively off at the lower frequencies.* On the other hand, even for zero drift

---

*As before, cf. Fig. 2.2 (Galubin's data), the behavior at 5 kHz departs from theory more noticeably than do the data at other (higher) frequencies. We suspect that this is the result of the small Rayleigh numbers involved, which reflect the fact that now contributions from the large-scale surface components are not entirely ignorable.

speeds the "classical" cases do not agree nearly as well with the data, and for larger drift speeds the discrepancies are quite pronounced. We can say, at least, that the soliton surface model, which is nondispersive, (cf. Sec. 1, Sec. 8.3) and hence exhibits disturbances moving at a constant speed, is consistent with the careful observations* of Roderick et al. [2], with respect to (mean) doppler shift. This is in addition to the plausibility of the model demonstrated by the backscatter data, as discussed above in Section 2.

4. Doppler Spread, ΔF: Theory and Experiment

The doppler spread, measured between $10 \log_{10} e^{-1}$ points below the spectral maximum in accordance with Eq. (10.10) and following the empirical procedure of Roderick et al. ([2], Fig. 14), is found from the analysis of Sec. 10 ff. (Part II) to be

$$\Delta F = \frac{\sqrt{2 \log \hat{C}\,(=10 \log_{10} e)}}{\pi} (2\alpha_{oz} k_o \sigma_{\dot{\zeta}}) \left\{ 1 + \frac{\sigma_\beta^2}{(2\alpha_{oz}\sigma_{\dot{\zeta}}/c_o)^2} + \frac{R_G}{k_o^2 (2\alpha_{oz}\sigma_{\dot{\zeta}})^2} \right\}^{\frac{1}{2}}, \tag{4.1}$$

which can be more compactly written

$$\boxed{\Delta F = A k_o \sqrt{1 + B + C/k_o^2}} \quad (= \sqrt{A^2 k_o^2 + A^2 B k_o^2 + A^2 C}\,), \tag{4.2}$$

where

$$\left.\begin{aligned} A &\equiv \frac{\sqrt{2 \log \hat{C}}}{\pi} (2\alpha_{oz}\sigma_{\dot{\zeta}}) = \frac{1.714}{\pi} (2\alpha_{oz}\sigma_{\dot{\zeta}}); \\ B &\equiv \sigma_\beta^2 / R_{\dot{\zeta}} = \sigma_\beta^2 \Big/ \left(\frac{2\alpha_{oz}\sigma_{\dot{\zeta}}}{c_o} \right)^2 ; \quad \text{where} \\ C &\equiv R_G / (2\alpha_{oz}\sigma_{\dot{\zeta}})^2 ; \quad R_G = (\text{Eq. } 8.29b)\,. \end{aligned}\right\} \quad \begin{aligned} &\sigma_{\dot{\zeta}}^2 = \text{Eq. (8.14)}; \quad \alpha_{oz} = \cos\theta_{oT} \\ &\sigma_\beta^2 = \hat{\sigma}_c^2 + \hat{\sigma}_d^2, \text{ Eq. (8.4)}; \end{aligned} \quad \begin{aligned} &(4.2a) \\ &(4.2b) \\ &(4.2c) \end{aligned}$$

Here the term ($\sim A k_o$) represents the phase modulation (of the carrier frequency f_o) which is produced by the random movement of the large-scale (i.e., gravity-capillary) wave surface, on which the soliton ensemble and drift layer move. The second term, involving $A^2 B$, embodies the phase modulation generated by the random variations ($\sim \sigma_c^2$) in the deep current

---

*See footnote, page 16.

speed and in the drift-current speed ($\sim\sigma_d^2$). Finally, the term A^2C gives the contribution of the amplitude modulation created by the random tilting of the local large-scale surface on which the small-scale components ride and move. Unlike the phase modulations here, this amplitude modulation is independent of the incident wave's frequency, cf. (4.2).

To determine σ_β^2 and R_G two spectral spread measurements are required. (In principle, we could calculate R_G if we knew how to truncate the point spectrum of the surface elevation ζ_G, cf. (8.27a), but this does not appear generally possible.) Thus, both σ_β^2 and R_G represent truly empirical, albeit physical quantities, to be found in practice by measurement, as we shall do here. Accordingly, if we select two different measurements of doppler spread ΔF_1, ΔF_2, for the given conditions of the experiment: $\overline{U_a}$, α_{oz}, k_o, $(\sigma_{\dot\zeta})_G$, appropriate to "high" frequencies $f_o \geqslant O(5\text{ kHz})$ and small grazing angles ($\theta_{oT} > 70°$), we can write from (4.2)

$$\Delta_1 = k_{o1}\sqrt{1 + B + C/k_{o1}^2}\ ;\quad \Delta_2 = k_{o2}\sqrt{1 + B + C/k_{o2}^2}\ ;\quad \Delta_{1,2} \equiv \Delta F_{1,2}/A. \tag{4.3}$$

Solving for B and C is routine. The results are

$$B = \frac{\Delta_2^2 - \Delta_1^2}{k_{o2}^2 - k_{o1}^2} - 1 \quad (> 0); \qquad C = \frac{\Delta_1^2 k_{o2}^2 - \Delta_2^2 k_{o1}^2}{k_{o2}^2 - k_{o1}^2} \quad (> 0), \tag{4.4}$$

since from (4.2b,c) B, C must be positive. We give several examples of the explicit calculations in Sec. 4.1 ff.

4.1 General Model I, Eqs. (4.1), (4.2): (Roderick's Experiments [2])

For the specific parameters of the recent experiments of Roderick et al. [2] we have

$$\theta_{oT} = 81°\ (\therefore \phi = 9°\text{ grazing angle});\ \text{mean wind speed } \overline{U_a} = 10\text{ m/sec};\quad c_o = 1.5 \cdot 10^3\text{ m/sec}. \tag{4.5a}$$

$$\therefore \sigma_{\dot\zeta}^2 = 2.09 \cdot \overline{U_a}^2 \cdot 10^{-3} = 0.209\ (\text{PM Spectrum, cf. Eq. (8.14)});\quad \therefore \sigma_{\dot\zeta} = 0.457; \tag{4.5b}$$

$$\alpha_{oz} = \cos\theta_{oT} = 0.157- \ ; \tag{4.5c}$$

$$\sigma_x^2 = 5.42 \cdot 10^{-2},\ \text{Eq. (8.10)};\ \therefore \sigma_x = 0.233; \tag{4.5d}$$

$$(\sigma_\zeta^2)_G = 1.42 \cdot 10^{-5}\,\overline{U_a}^4 = 0.142\ (m^2);\ \therefore (\sigma_\zeta)_G = 0.377. \tag{4.5e}$$

$$\therefore A = \frac{1.714}{\pi}(0.313)(0.457) = \boxed{7.82 \cdot 10^{-2}}; \quad \boxed{B = \sigma_\beta^2/(9.54 \cdot 10^{-8})} \quad \boxed{C = R_G/(2.05 \cdot 10^{-2})} \quad (4.6)$$

The elements of the calculations based on (4.4) are given in Table 4.1:

Table 4.1 Calculated Doppler Spreads, $\Delta F_{(\ )}$

				← Expt'l →		Curve(s) I.	Fig. 4.1
f_o	ΔF (Xpt'l;[2], Fig. 14)	k_o	k_o^2	$\Delta_{(f_o)} = \frac{\Delta F}{A}$	$\Delta^2_{(f_o)}$	$\therefore \Delta F_{10,20}$	$\Delta F_{5,20}$
20 kHz	23.7 Hz	83.78	7019	$3.03 \cdot 10^2$	$9.185 \cdot 10^4$	23.7 Hz	23.7 Hz
15	22.0	62.84	3949	$2.81 \cdot 10^2$	$7.915 \cdot 10^4$	(20.6)	(20.4)
10	18.0	41.89	1755	$2.30 \cdot 10^2$	$5.298 \cdot 10^4$	18.0	(17.4)
5	15.0	20.95	439	$1.92 \cdot 10^2$	$3.679 \cdot 10^4$	(16.3)	15.0

( ) = calculated from (4.3), based on ΔF_{10}, ΔF_{20}, or ΔF_5, ΔF_{20}, as indicated.

Table 4.1a Auxiliary Parameters, Eq. (4.4)

	$B_{10,20}$	$10^{C_{20}}$	$B_{5,20}$	$5^{C_{20}}$
	6.38	$4.00\ 10^4$	8.37	$3.32\ 10^4$
$\therefore \sigma_\beta$	$7.83 \cdot 10^{-4}$ rad	--	$8.94 \cdot 10^{-4}$ rad	--
$\therefore R_G$	--	$8.20 \cdot 10^2 \text{sec}^{-2}$	--	$6.81 \cdot 10^2 \text{sec}^{-2}$
ΔF_{AM} = Eq. (4.8)	--	15.6 Hz	--	14.2 Hz
$\Delta F_\beta \equiv f_o \sigma_\beta$	15.7 Hz	--	17.9 Hz	--

The results of applying (4.3) are shown in Fig. 4.1; the solid curve (for I ≡ Model I) is based on the selection of the two data points ΔF_{20} = 23.7 Hz and ΔF_{10} = 18.0 Hz, where the calculated points, following this choice of ΔF_{20}, ΔF_{10}, are indicated by the circled numbers in Table 4.1. Similarly, the calculated points in the dotted curve (Model I) are obtained

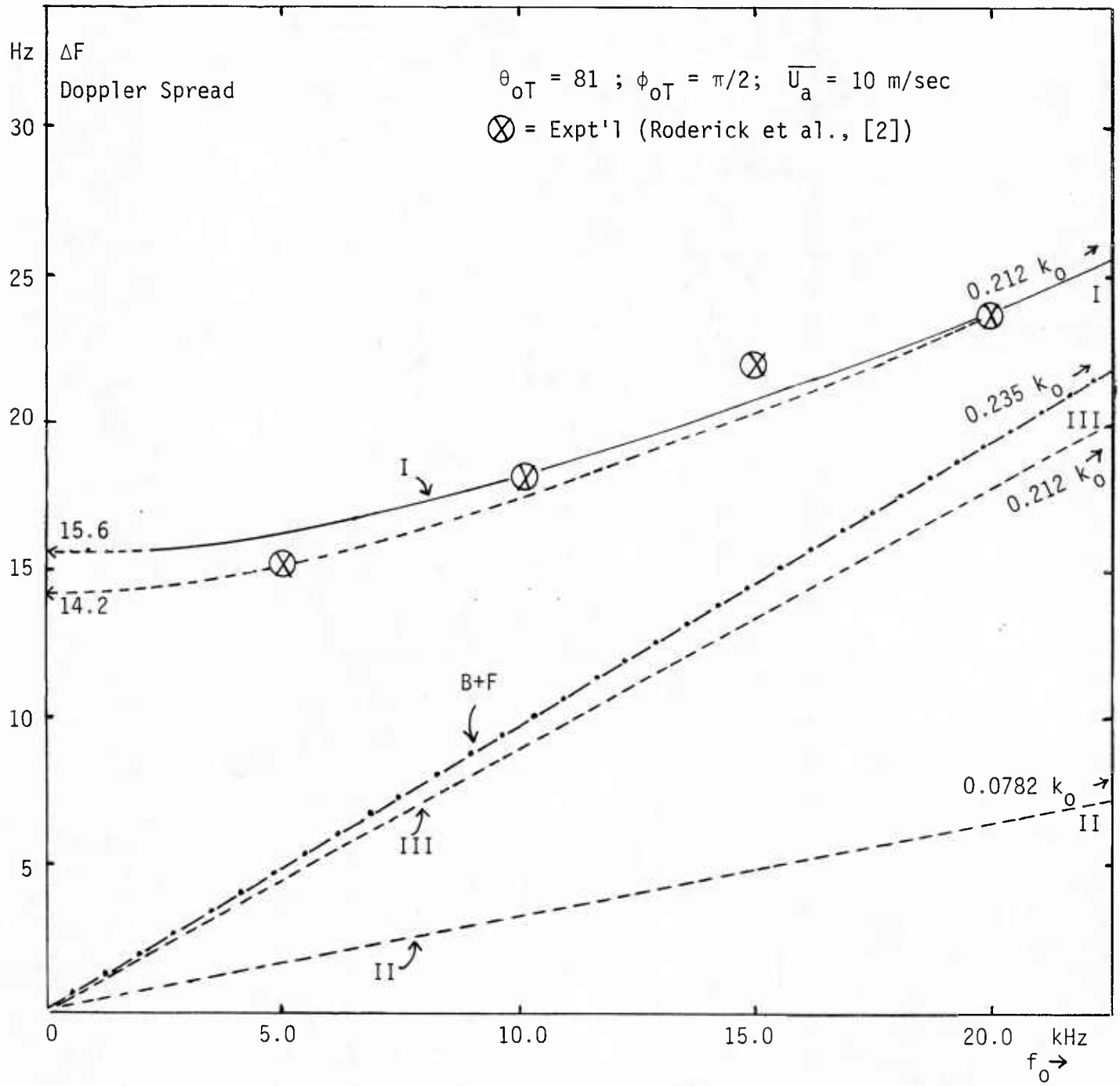

Figure 4.1 Doppler spread ΔF, theory and experiment, Eq. (4.1), (4.2), for the soliton model. Classical (gravity-wave) and other results (4.9) and Table 4.2.

from the selection of ΔF_{20}, ΔF_5. The fit appears better for the first choice (solid line); our selection of ΔF_{20}, in any case, is reasonable, as this result is probably more accurate than the others, both from the experiment and from the fact that f_o is larger and therefore the observed $\Delta F_{(20)}$ is more accurate.

The auxiliary quantities B, C are shown in Table 4.1a, along with estimated values of σ_β and R_G. If we define a measure of spectral spread (not the same as used in (4.1) et seq., cf. Eq. (10.10), but proportional to it) by

$$\Delta F_\beta \equiv f_o \sigma_\beta, \quad \text{cf. (8.3)} , \tag{4.7}$$

we see (Table 4.1a) that at f_o = 20 kHz the rms spread due to the combined effects of deep current and drift velocity variation is O(16 Hz). Similarly, we see that if the spread due to the AM effects of the random tilt is defined by

$$\Delta F_{AM} \equiv \lim_{k_o \to 0} \Delta F = A \sqrt{C} = \frac{1.714}{\pi} \sqrt{R_G} , \tag{4.8}$$

then the resulting doppler spread due to this mechanism is O(14, 15 Hz), cf. Table 4.1a. [The overall resultant doppler spread, as given by (4.1), (4.1), of course, is not simply the sum of the individual spreads, because of the way the various spreading mechanisms interact physically, vide Secs. 8-10.]

As frequency becomes less, our results (4.1) approach a nonvanishing value. This, of course, does not actually occur physically below some $f_o \sim$ O(+2 kHz), where the dominant Bragg scatter term is now that of the large-scale component (not evaluated here). Thus, our results for Model I here are not to be extrapolated to frequencies below O(1-2 kHz). On the other hand, for frequencies much above 20 kHz the spatial terms in $F_{2\text{-}G}$, (8.8), appear as they do in the tilt factor, $K_{N(0)}(\underline{\Delta r},\tau)$, cf. (7.5a). We no longer have a simple soliton "wave" surface, but one (cf. Σ in (7.8) et seq.) where the dispersion law K_Σ is no longer simple. This changes the doppler shift, δf_o, cf. Sec. 7. (vs. Secs. 7.2, 7.3), but does <u>not</u> change the τ-structure of $M^{(0)}_{RT}(\tau|f_o)$, cf. (10.3)-(10.7), where $K_s \to K_\Sigma$, $W_s \to W_\Sigma$ now: the scale of $W_{X-\langle X\rangle}$ is altered, <u>but not the spreading terms</u>

($\sim \sigma_\Delta^2$), (10.2). We conclude, therefore, that as frequency (f_o) is increased, i.e., as $k_o \to \infty$, Equation (4.1) (and (4.2)) still provide the measure of doppler spread, i.e., $\lim_{k_o \to \infty} \Delta F \to A k_o \sqrt{1+B} \sim 0.212\ k_o$, cf. Fig. 4.1. Moreover, at very high frequencies, the backscatter cross section $\hat{\sigma}_S^{(0)}$, (2.6), becomes independent of frequency; [whereas, as $k_o \to 0+$, $\hat{\sigma}_S^{(0)} \sim k_o^4$, albeit that this effect is overwhelmed by an analogous Bragg scatter from the gravity-capillary component.]

Finally, Fig. 4.1 also shows our Models II, III, where we have respectively dropped the contributions ($\sim$ B, C) and ($\sim$ C), in (4.2). Table 4.2 lists pertinent values of ΔF calculated for these models, with the parameters (4.5), (4.6):

Table 4.2 Simplified Doppler Spread Models

f_o	k_o	(I). $\Delta F = A k_o$	(II). $\Delta F = A k_o \sqrt{1+B}$
20 kHz	83.78	6.55 Hz	17.8 Hz
15	62.84	4.91	13.3
10	41.89	3.28	8.81
5	20.95	1.64	4.41

Clearly, without the AM contribution, the results are nowhere near those observed empirically.

4.2 A Classical Model: Bass and Fuchs et al. [29]

Here we take Eq. 15 of [29] and use the same criterion (10.10) for spectral spread as above. The resulting doppler spread for this "classical" case is accordingly (with $\Gamma_{B+F} \equiv \sqrt{\sigma_x^2 + \sigma_y^2} = \sqrt{2}\,\sigma_x$ here)

$$\Delta F_{B+F} = 2\alpha_{oz} k_o \frac{\sqrt{2^{1/4} g}}{\sqrt{\pi}} \sqrt{\sigma_\zeta \sigma_x} \sqrt{\log \hat{C}}, \qquad \log \hat{C} = 1.468, \tag{4.9}$$

where as before, cf. (4.1), it is the interface motion which causes the doppler, and doppler spread. [If, instead, we consider the particle

motion adjacent to the interface to cause the doppler, as Bass, Fuchs et al. [29] do, then we must replace α_{oz} in (4.9) by unity, e.g.,

$$\Delta F'_{B+F} = 2k_o \frac{\sqrt{2^{1/4}g}}{\sqrt{\pi}} \sqrt{\sigma_\zeta \sigma_x} \sqrt{\log \hat{C}} \quad . \tag{4.9a}$$

However, it is the moving wave interface, with its very large ρc_o contrast vis-à-vis that of the fluid flow of the particles producing the wave motion ultimately (with $\rho c_o \sim 1$, where the net fluid flow vanishes), which clearly dominates. Moreover, without the factor α_{oz} here in (4.9), the resultant ΔF is much too large, cf. Table 4.3 ff.]

For the present experiment, using again the PM spectrum (1.1) and the data of (4.5) above, we get directly

$$\Delta F_{B+F} = 0.235\ k_o \quad (\text{and } \Delta F'_{B+F} = 1.51\ k_o), \tag{4.10}$$

shown in Table 4.3 and Fig. 4.1.

Table 4.3 ΔF_{B+F}; $\Delta F'_{B+F}$

f_o	k_o	ΔF_{B+F}, Eq. (4.9)	$\Delta F'_{B+F}$, Eq. (4.9a)
20 kHz	83.78	19.6 Hz	1.26 10^2 Hz
15	62.84	14.7	94.6
10	41.89	9.80	63.1
5	20.95	4.90	31.5

5. Results and Conclusions

In the preceding Sections we have shown that our theoretical surface scattering model, employing the wind-generated soliton ensemble postulated by the author in recent work [1]-[3], accounts very well for the observed data [2]. This is true not only for the measured backscatter cross sections $\hat{\sigma}^{(0)}_{incoh}$, cf. Fig. 2.2, but for the mean doppler shift, δf_o, Fig. 3.1, and the doppler spread, ΔF, in Fig. 4.1. Indeed, a noteworthy feature of the model and the analysis based on it is the excellent internal consistency demonstrated in the results calculated

from it. For example, the parameters indicated by the fit of theory and experiment in the backscatter evaluation, e.g., σ_h for instance, are consistent with the soliton ensemble (cf. Sec. 9) and the approximations involved in determining the doppler spread component arising from the wave motion of the large-scale surface [Sec. 8.2]. Similarly, our model can account for the observed doppler spread ΔF, which is noticeably different from the theoretical predictions based on classical approaches (Sec. 4.2), and indeed, from analyses here which omit the critical amplitude modulation, caused by the random tilting of the large-scale surface component.

We emphasize that the soliton surface model used here is not conclusively established by the experimental data [2]. Nevertheless, it is both plausible physically (cf. Secs. 1, 9) and capable of predicting simultaneously such key quantities as (back)-scatter cross sections ($\hat{\sigma}^{(0)}$), doppler shift (δf_o), and doppler spread (ΔF) over a wide range of frequencies (5-20 kHz here, and beyond). Indeed, with such a model we have also demonstrated that the underwater acoustic measurement techniques of Roderick et al. [2] are fully capable of quite accurately determining these key quantities ($\hat{\sigma}^{(0)}$, δf_o, ΔF). (We expect similar results for the intensity spectrum, $W_{\chi-\bar{\chi}}$, as well.) These results, of course, are pertinent to the particular physical conditions noted earlier (Sec. 1), namely: (i), an effectively "bubble-free" environment in the near-surface region [cf. discussion in Sec. 2]; (ii), high frequencies (i.e., large Rayleigh numbers); and (iii), small grazing angles. When wind-wave interactions are such as to produce significant bubble densities and distributions, the latter will dominate and the soliton surface mechanism will not be observable.

It is instructive to compare our present model, vis-à-vis experiment, with the various other models proposed earlier and currently (see [1], Sec. 3.2, for example, and [5], [9]). We do this qualitatively in Table 5.1.

The classical models [(1), (2) in Table 5.1] are almost completely inadequate to account for the observed values of $\hat{\sigma}^{(0)}_{inc}$, δf_o, ΔF under the conditions of the Roderick experiments [2], which operated in a "bubble-

Table 5.1 Comparison of Scatter Models with Experiment*
(High Frequencies and Small Angles)

Model	$\sigma^{(0)}_{inc}$	δf_o	ΔF	Remarks: Physical Mechanisms
1. Classical: grav. + capil. waves--no bubbles; [9], [18], see [1], Sec. 3.	No; O(15-20 db) too low	No; (see Fig. 3.1)	No; too low; (cf. Fig. 4.1)	Linear wave generation: dispersive; staurated spectrum, cf. (1.1)
2. Same as 1.--C→ C($\overline{U_a}$, var U_a, etc.) ([13]-[15]; Sec. 1.2 here. Eq. (1.1).)	Yes	No; (Fig. 3.1)	No; (Fig. 4.1) too low	C made larger, cf. Eq. (1.1); dispersive; Linear wave generation; unsat. spectrum
3. Classical + assumed bubble layer; [5], [6], [9]; Sec. 2 here.	Yes	No. (no doppler shift)	No. AM masked	Not appropriate when bubbles are ignorable, cf. Sec. 2; dispersive; depends on wind-wave interactions; lin. wave generation
4. Soliton Surface Ensemble (+ classical): [1]; this Report.	Yes (Fig. 2.2)	Yes (Fig. 3.1)	Yes (Fig. 4.1)	Nonlinear mech. Consistent with wind-wave generation, [3], [4], [32]. Nondispersive.

*High frequencies, small grazing angles, etc., cf. Secs. 1, 2. , and [1], and "bubble-free" régimes, cf. last part of Sec. 2.

free" régime [cf. remarks at end of Sec. 2 above]. In the unsaturated cases [$C \to C(\overline{U_a}$, var U_a, ...) as $\omega_s \to \infty$, cf. Sec. 1.2] it may be possible to achieve the observed values of $\hat{\sigma}^{(0)}_{inc}$ with this model, but the model is incapable of providing the observed values of doppler (δf_o, ΔF). A similar situation arises with model (3), in addition to which there are no observed bubbles effective in masking the scattering surface, for the environmental condition of the experiments involved. Models (1)-(3) are all dispersive in their surface wave production, which recent work ([3], [4], [25], [32]) suggests is not the dominant effect at these frequencies. For "bubble-free" régimes, our present model (4), which involves non-dispersive surface propagation, on the other hand, is entirely able to account for the observed data and predict other values, at different frequencies, grazing angles, etc. (consistent, of course, with the high-frequency, small-angle conditions postulated throughout).

To sum up, we have followed the philosophy of constructing a plausible scattering mechanism which is strongly suggested by the governing nonlinear physics of wind-wave interactions ([3], [4], [32] and Sec. 9 here). We then use the data from careful experiments [2], with particular attention to the "ground-truth" involved, viz., geometry, wind speeds, currents, etc., to determine the numerical value of the model parameters. With these available, the model becomes predictive for other operating conditions, under the same general constraints of small grazing angles, high frequencies, and "bubble-free" nonsurface environments.

Our scatter mechanism is naturally described by a three-parameter model (σ_h, σ_S, c_s, cf. (9.7) or (9.9)), in the covariance or spectrum, unlike the classical cases, which involve two-parameter models (C, $\overline{U_a}$, cf. (1.1)) in the point-spectrum, for example). This added versatility helps the model to account for the variety of different observed data and enhances its capabilities for prediction, consistent with the inherent physical mechanisms which govern the scattering process. Although the soliton surface ensemble postulated in our current treatments [1], [3], [4], [32] has not yet been directly observed, our new results (Secs. 2-4) taken in conjunction with the wind-wave interaction model [4], [8], [32], provide inferentially very strong support for the existence of this surface scattering mechanism. As can be seen from Table 5.1, the various "perturbations" of the classical linear surface model fail to amount adequately for the observed phenomena.

Part II. Analysis

6. The Intensity Spectrum of the Received Scatter: (High Frequency Régimes)

To determine the rôle of doppler produced by the moving wave surface, we must first obtain the intensity spectrum of the scattered returns. Accordingly, our analysis is based on the results of Section 7 of [1], in particular Sec. 7.3B. Here we need to make a variety of modifications to include the effects of the various doppler components of our physical model (cf. Sec. 3), specifically to account now for the temporal as well as spatial variability of the complex moving wind-water interface. As before [1], we are concerned here only with the cases of high frequencies ($f_o \geq 5$ kHz) and small grazing angles ($\theta_{oT} > 65°$), so that the "facet" or geometrical optics terms, along with the Bragg scatter from the capillary components, may be ignored vis-à-vis the surface soliton scatter terms (Secs. 1, 2 of [1] and Secs. 1, 2 here).

Although the correlation distance, ℓ_s, of the small-scale scatterers is small compared to that of the large-scale (gravity) wave surface, we cannot now neglect the temporal correlation effects in the latter in that they contribute to doppler spread, as we shall see below. Moreover, in addition to the various random frequency modulations produced by the movement of the small-scale surface components, we also cannot neglect the amplitude modulation of the Bragg scatter wave surface components by the large-scale gravity waves, which is manifested in the time-variability of the "tilt-factor" $N^{(0)}_{GS\text{-}inc}$. Although this latter is comparatively slow, it exhibits an important, frequency-independent contribution to the doppler spread, which is consistent with Roderick's data [2], Fig. 14, and Fig. 4.1 here. Finally, we must include the mean doppler components, which represent the doppler shifts (δf_o) arising from the steady movement of subsurface and surface current, and soliton movement on the moving wave surface itself.

With the above in mind, we may apply (7.28) in (7.34), (7.34a), (7.35) of [1], bypassing (7.31) and noting that now $N^{(0)}_{GS\text{-}inc}$ in (7.34a) depends on the time-difference $\tau = t_2 - t_1$, as well as on vertical angle θ_{oT}. With the help of [23] for the deterministic doppler terms, and

remembering that the intensity spectrum is given by

$$W_Y(f) = 2F_t\{M_Y(\tau)\} = 2\int_{-\infty}^{\infty} e^{-i\omega\tau} M_Y(\tau)d\tau = W_Y(f), \quad \omega = 2\pi f, \tag{6.1}$$

cf. [24], Eq. (3.42) et seq., we may write the extended version of (7.34), (7.34a) here for the received incoherent scatter return, X-<X>, as

$$\boxed{W_{X-\langle X\rangle}(f) = 2\int_{-\infty}^{\infty} e^{-i\omega\tau}\ \mathrm{Re}\left\{k_o^2 G^{(1)} K_o(\tau)_{in} e^{-i\omega_o\tau}\ M_{RT}^{(0)}(\tau)\right\} d\tau,}$$

$$\tau = t_2 - t_1, \quad f \geq 0-, \tag{6.2}$$

where

$$G^{(1)} \equiv \frac{e^{-2a\omega_o^2 c_o T_o}}{(4\pi)^2 R_{oT}^2 R_{oR}^2} \quad \text{("geometric" or spreading factor, cf. (7.11a) [1], and Fig. 5.2, [1]; } T_o = (R_{oT}+R_{oR})/c_o; \tag{6.2a}$$

$$K_o(\tau)_{in} = \int_{-\infty}^{\infty} w_{in}(f')e^{-i\omega'\tau}df'; \quad w_{in}(f') \equiv \frac{A_o^2}{2}\left|S_{in}(f')\right|^2, \quad f' = f - f_o, \text{ for narrow band signals, cf. (7.11b), [1],} \tag{6.2b}$$

and also

$$\omega_o = 2\pi f_o; \quad f_o = \text{"carrier" or central signal frequency;}$$

$$k_o = 2\pi/\lambda_o = 2\pi f_o/c_o = \omega_o/c_o, \tag{6.2c}$$

where, as before, c_o is the (average) speed of sound in the water medium. (In this definition, (6.1) above, of spectrum, only nonnegative frequencies are defined.)

Specifically, $M_{RT}^{(0)}(\tau)$, (7.34a,b), (7.35), [1] is now modified to be, for these cases of high frequency and small grazing angles,

$$M_{RT}^{(0)}(\tau) \doteq \overline{R_o^2}\,\overline{S^2}\,k_o^2\left[g_T g_R \frac{A_1}{2}\right]\iint_{[\Delta r]} \underbrace{\left\langle e^{ik_o 2\underset{\sim}{\alpha}_o\cdot\underset{\sim}{v}_D^2\tau}\right\rangle_D}_{①} \underbrace{e^{-\hat{A}_T\Delta r^2/4}}_{②} \cdot e^{2ik_o\underset{\sim}{\alpha}_o\cdot\underset{\sim}{\Delta r}}$$

$$\cdot\, K_S(\underset{\sim}{\Delta r},\tau)\underbrace{K_{N(0)}(\underset{\sim}{\Delta r},\tau)}_{③}\underbrace{\left\langle e^{2ik_o\underset{\sim}{\alpha}_o\cdot(\underset{\sim}{\zeta}_2-\underset{\sim}{\zeta}_1)_G}\right\rangle_G}_{④} d(\underset{\sim}{\Delta r});\quad \underset{\sim}{\Delta r} = r_2 - r_1. \tag{6.3}$$

Here we note the following changes introduced into (7.35), [1]:

① $\exp(ik_o 2\underset{\sim}{\alpha}_o\cdot\underset{\sim}{v}_D\tau)$: This represents the doppler shift ($\sim \underset{\sim}{v}_D$), stemming from the velocity components of various moving scattering elements, etc. The anatomy of $\underset{\sim}{v}_D$ is described in Section 7 ff.: it consists of a mean term (= doppler shift) and a fluctuation component $\underset{\sim}{\Delta v}_{oD}$, which produces a random phase modulation and spectral spread. The average $\langle\,\rangle_D$ is over these random terms. (6.4a)

② $e^{-\hat{A}_T\Delta r^2/4}$: This term is $I_3(\underset{\sim}{\Delta r})$, (6.40), [1], and stems from the fact that $I_3(0)$ in (7.35), [1] is replaced by $I_3(\underset{\sim}{\Delta r})$, to prevent possible singularities in the integration over $\underset{\sim}{\Delta r}$ in (6.3). [As we shall see later, cf. Sec. 10, $\hat{A}_T$ proves to be sufficiently small and the integrations devoid of singularities, that $\hat{A}_T = 0$ without noticeable effect on our results.] (6.4b)

③ $K_{N(0)}(\underset{\sim}{\Delta r},\tau)$: This replaces $N_{G\text{-inc}}^{(0)}(\underset{\sim}{\alpha}_o)$ in (7.35), [1], is given in (7.28), [1], and represents the above-mentioned amplitude modulations by the large-scale (gravity) wave surface. This covariance function is evaluated in Sec. 8.3 ff. (6.4c)

④ $$\left\langle e^{2ik_o \underset{\sim}{\alpha}_o \cdot (\underset{\sim}{\zeta}_2 - \underset{\sim}{\zeta}_1)_G} \right\rangle_G \equiv F_2(-2ik_o\alpha_{o2},\ 2ik_o\alpha_{o2};\ \underset{\sim}{\Delta r}, \tau)_G : \tag{6.4d}$$

$$= \exp\left\{-4\sigma_G^2 k_o^2 \alpha_{oz}^2 \left[1 - \rho_G(\underset{\sim}{\Delta r}, \tau)\right]\right\}, \tag{6.4e}$$

for the gaussian gravity wave elevation ζ_G; (we neglect the small doppler corrections noted in (7.29), [1]). This is appropriately approximated in Sec. 8.2 ff.

Here $K_S(\underset{\sim}{\Delta r}, \tau)$ is the space-time covariance of the soliton ensemble which provides the effective scattering mechanism in our present model, including the (mean) doppler shift due to Bragg scattering, cf. Sec. 7 ff. The explicit structure of K_S is developed in Sec. 8.4 ff., based on [3], [4]. The vector quantity $2\underset{\sim}{\alpha}_o$ is given by (5.24), [1], and for the backscatter geometry considered here (cf. Fig. 2.1 and Figs. 2.2a, 5.1 of [1]), becomes explicitly

$$2\underset{\sim}{\alpha}_o = 2\hat{\underset{\sim}{i}}_x \cos\phi_{oT} \sin\theta_{oT} + 2\hat{\underset{\sim}{i}}_y \sin\phi_{oT} \sin\theta_{oT} + 2\hat{\underset{\sim}{i}}_z \cos\theta_{oT}. \tag{6.5}$$

Other pertinent quantities in (6.3) are:

$\frac{A_1}{2} = A_{REF}$ = reference area, Eq. (2.11), [1], used in the definition of the scattering cross section, cf. Sec. 2.2 of [1]. (6.6a)

g_T, g_R = beam "gains," cf. (6.17), [1]. (6.6b)

The various approximations on which (6.2), (6.3) above are based are cited in Sec. 5.5, [1]. The principal ones are:

(i). (local) stationarity and homogeneity of (at least) the large-scale wave surface;
(ii). narrow-band signals;
(iii). far-field (i.e., Frauenhofer region) operation;
(iv). small dopplers and slowing moving surfaces (vis-à-vis c_o);
(v). gaussian statistics for $\zeta(\underset{\sim}{r}, t)_G$, as noted in (6.4c);
(vi). narrow "beams" (or at least one (T or R) narrow beam); cf. Sec. 6, [1]. (6.7)

(For others, see the derivations in Sec. 7.3, [1], leading to (7.35).)

Our immediate next steps are, accordingly, to construct a doppler model (Sec. 7); to evaluate $F_{2\text{-}G}$, (6.4d,e), appropriate to the integrand of (6.3), (Sec. 8.2); to obtain (Sec. 8.3) an appropriate structure for $K_N(0)$, cf. (6.4c); and then to construct the surface soliton covariance K_S, (Sec. 9), in the light of our most recent work, [3], [4], which supercedes the initial (and limited) model originally presented in Sec. 3B of [1]. Finally, in Section 10 ff. we evaluate the doppler spread, ΔF, for our model, summarizing in Section 4.2 earlier corresponding results based on the purely "classical" model where the scattering mechanism is provided by the gravity-capillary surface alone.

7. The Mean Doppler Shift: Analysis

The deterministic velocity $\underset{\sim}{v}_{oD}$ in Eq. (6.4a) represents the sum of the mean (or transport) velocities associated with the various moving fluid elements of the physical environment of Roderick's experiment [2]. Specifically, these are: (1) a noticeable deep layer current, extending from the surface to the bottom, O(21 cm/sec), and (2) the surface drift layer, produced by the wind upon the wave surface. In addition, there is a doppler shift generated by the soliton-ensemble, in our present model, which constitutes the moving water-atmosphere interface. This is the effective Bragg-scatter component here, which as we have shown earlier ([1], Secs. 2, 3), and Fig. 2.2 of Section 2 above) is the dominant contributor vis-à-vis the ultra-gravity and capillary elements of the wave surface.

The doppler velocities for the elements of the moving mechanisms (1) and (2) are represented by

$$\underset{\sim}{v}_D = \hat{\underset{\sim}{i}}_c v_c + \hat{\underset{\sim}{i}}_d v_d, \tag{7.1}$$

which we can rewrite as

$$\underset{\sim}{v}_D = \underset{\sim}{v}_{oD} + \underset{\sim}{\Delta v}_D; \quad \underset{\sim}{v}_{oD} = \hat{\underset{\sim}{i}}_c \underset{\sim}{v}_c + \hat{\underset{\sim}{i}}_d \underset{\sim}{v}_d; \tag{7.2}$$

$$\underset{\sim}{\Delta v}_D = \hat{\underset{\sim}{i}}_c (v_c - \overline{v_c}) + \hat{\underset{\sim}{i}}_d (v_d - \overline{v_d}) = \text{velocity fluctuations.}$$

The deterministic portion, $\underset{\sim}{v}_{oD}$, is responsible for doppler shift contributions, while the velocity fluctuations, $\underset{\sim}{\Delta v}_D$, contribute to the doppler spread, ΔF, cf. Sec. 8 and Sec. 10 ff. Figure 7.1 shows the present doppler geometry, along with that of the surface wave number $\underset{\sim}{\nu} = [\underset{\sim}{k}/2\pi = (\nu,\phi_\nu) = (\nu_x,\nu_y)]$, and the transmitter-receiver configuration for backscatter here. It is assumed in our present model that:

(i). all doppler velocities lie essentially in the plane of $\zeta = 0$ (equil. wave surface) or planes parallel to it;
(ii). all dopplers are small: $|\underset{\sim}{v}_D|_{max} << c_o$, etc.;
(iii). $-\pi/2 \leq \phi_\nu = \Phi_w \leq \pi/2$: waves can go forward in the direction of the wind, over an angular domain π radians in extent;
(iv). the drift layer velocity is essentially in the mean wind direction, i.e., $\phi_d = \Phi_w$, cf. Fig. 7.1;
(v). the surface wave numbers $\underset{\sim}{\nu}$ lie, essentially, in the (x,y)- or (ζ=0)-plane, cf. Fig. 7.1. (7.3)

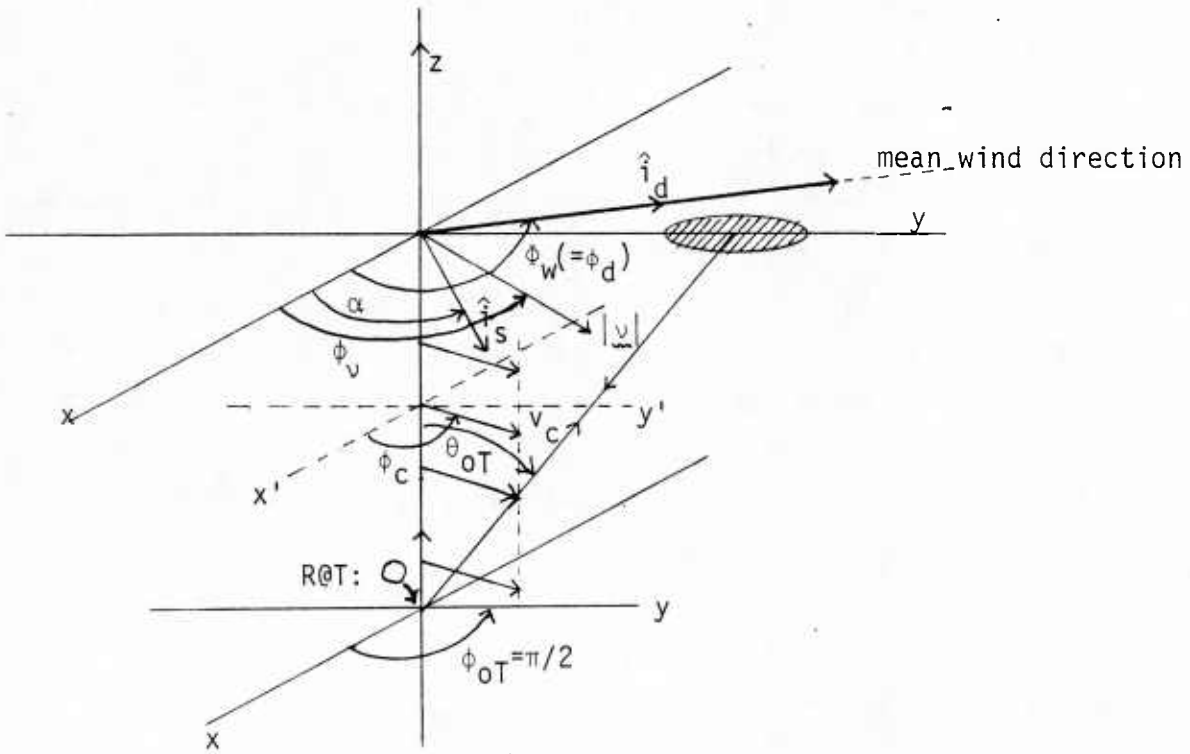

Figure 7.1: Geometry of the fluid transport dopplers (deep current and surface drift), backscatter, and surface wave numbers.

The unit vectors of (7.1), (7.2), cf. Fig. 7.1, are given by the following relations:

$$\hat{\underset{\sim}{i}}_c = \hat{\underset{\sim}{i}}_x \cos\phi_c + \hat{\underset{\sim}{i}}_y \sin\phi_c; \quad \hat{\underset{\sim}{i}}_d = \hat{\underset{\sim}{i}}_x \cos\Phi_w + \hat{\underset{\sim}{i}}_y \sin\Phi_w, \tag{7.4a}$$

while for subensembles of solitons moving in the direction $\hat{\underset{\sim}{i}}_S$, we have

$$\hat{\underset{\sim}{i}}_S = \hat{\underset{\sim}{i}}_x \cos\alpha + \hat{\underset{\sim}{i}}_y \sin\alpha \ . \tag{7.4b}$$

The solitons comprising the wave surface interface all move in the direction of the wind, i.e., $-\pi/2 \leq \alpha - \Phi_w \leq \pi/2$ here, just as the gravity-capillary surface waves do, and like the latter, they move anisotropically on the surface, subject to some distribution law

$$w_1(\alpha) = A_n \cos^n\alpha \ , \quad -\pi/2 \leq \alpha - \Phi_w \leq \pi/2, \quad A_n = \langle \cos^n\alpha \rangle_\alpha^{-1} \ , \tag{7.4c}$$

typically.

7.1 Resonant (or Bragg) Scatter: General Doppler Shift, I

Equation (6.2), with (6.3), is precisely the dominant Bragg, or resonant scatter term, at the high frequencies and small grazing angles of interest here.

To demonstrate the doppler shift δf_o explicitly, let us rewrite (6.3) more compactly as

$$M_{RT}^{(0)}(\tau) = B \iint_{[\underset{\sim}{r}]} K_\Sigma(\underset{\sim}{\Delta r},\tau) \left\langle e^{2ik_o \underset{\sim}{\alpha}_o \cdot \underset{\sim}{v}_o D\tau} \right\rangle_D e^{2ik_o \underset{\sim}{\alpha}_o \cdot \underset{\sim}{\Delta r}} \, d(\underset{\sim}{\Delta r}) \tag{7.5}$$

where

$$K_\Sigma = K_{N(0)}(\underset{\sim}{\Delta r},\tau) F_2(\underset{\sim}{\Delta r},\tau)_G K_S(\underset{\sim}{\Delta r},\tau) e^{-\hat{A}_T \Delta r^2/4} \tag{7.5a}$$

is the product covariance of the various covariances of the effective scattering surface Σ, cf. (6.3), (6.4). This effective scattering surface Σ is a "product" surface, not simply formed as a linear superposition of surface wave components, generally. Nevertheless, the integral

in (7.5) is just the wave number-time intensity spectrum associated with $K'_\Sigma \equiv K_\Sigma \cdot \langle \exp(2ik_o \underset{\sim}{\alpha}_o \cdot \underset{\sim}{v}_{oD} \tau) \rangle_D$, viz.:

$$\Phi_\Sigma(\underset{\sim}{\nu}_o, \tau) \equiv F^{-1}_{\underset{\sim}{\Delta r}}\{K'_\Sigma\} = \iint_{[\underset{\sim}{\Delta r}]} K_\Sigma(\underset{\sim}{\Delta r}, \tau) e^{2ik_o \underset{\sim}{\alpha}_{o\perp} \cdot \underset{\sim}{v}_{oD} \tau} \cdot \left\langle e^{2ik_o \underset{\sim}{\alpha}_{o\perp} \cdot \underset{\sim}{\Delta v}_D \tau} \right\rangle_D e^{2ik_o \underset{\sim}{\alpha}_o \cdot \underset{\sim}{\Delta r}} \, d(\underset{\sim}{\Delta r}) = M^{(0)}_{RT}(\tau)/B, \tag{7.6}$$

where we have used (7.2) to extract the mean doppler term ($\sim \underset{\sim}{v}_{oD}$) from the doppler average $\langle \rangle_D$ explicitly. Here, in particular, we write

$$\boxed{\underset{\sim}{\nu}_o \equiv 2k_o \underset{\sim}{\alpha}_{o\perp}/2\pi = \frac{k_o}{\pi}(\hat{\underset{\sim}{i}}_x \cos\phi_{oT} \sin\theta_{oT} + \hat{\underset{\sim}{i}}_y \sin\phi_{oT} \sin\theta_{oT});}$$

$$\underset{\sim}{\alpha}_{o\perp} = (\underset{\sim}{\alpha}_o)_{x,y}, \tag{7.7}$$

from (6.5): there is no z-component of $\underset{\sim}{\alpha}_o$ in $\underset{\sim}{\nu}$, since $\underset{\sim}{\Delta r}$ lies solely in the (x,y)-plane. In general, $\underset{\sim}{\bar{v}}_{oD}$ and $\underset{\sim}{\Delta v}_D$ may depend on position.

Next, we use the fundamental relation between the point-(intensity) frequency spectrum W'_Σ of an anisotropic surface, and its directional covariance function, $K'_\Sigma(\underset{\sim}{\Delta r}, \tau)$, [26]:

$$\boxed{K'_\Sigma(\underset{\sim}{\Delta r}, \tau) = \int_0^\infty W'_\Sigma(f_s) \left\langle \cos[\omega_s \tau - \underset{\sim}{K}^{(\alpha)}_{\Sigma'}(f_s) \cdot \underset{\sim}{\Delta r}] \right\rangle_\alpha df_s,} \qquad \omega_s = 2\pi f_s, \tag{7.8}$$

with

$$\underset{\sim}{K}^{(\alpha)}_{\Sigma'} \cdot \underset{\sim}{\Delta r} = K_{\Sigma'} \Delta r \cos(\phi_\nu - \alpha), \tag{7.8a}$$

in polar coordinates.* Here $K^{(\alpha)}_{\Sigma'}(f_s)$ embodies the dispersion law (relating wavelength, λ_Σ, ($\sim K^{-1}_{\Sigma'}$) to wave frequency f_s) of the "product" surface Σ', whose covariance of elevation ($\zeta_{\Sigma'}$) is given by (7.5a) above including the doppler term, cf. 7.6. [In general, $W_{\Sigma'}$ is complex in this formulation. However, without much loss of generality, if we can regard

---

*Although Σ is generated nonlinearly, cf. (7.5a), it can be spectrally decomposed linearly, i.e., by the usual Fourier methods.

$\bar{\underset{\sim}{v}}_{oD}$ as independent of $\underset{\sim}{\Delta r}$, and $\langle \exp(2ik_o \alpha_{o\perp} \cdot \Delta v_D \tau) \rangle_D$ as real; then W_Σ, is also real-positive.]

Accordingly, we shall assume here and subsequently that $\bar{v}_{oD}$ and $\underset{\sim}{\Delta v}_D$ are independent of $\underset{\sim}{\Delta r}$. Then, applying (7.8) in (7.6) gives

$$\left.\begin{aligned} \Phi_\Sigma(\underset{\sim}{\nu}_o, \tau) = \left\langle e^{2ik_o \underset{\sim}{\alpha}_{o\perp} \cdot \underset{\sim}{\Delta v}_D \tau} \right\rangle_D \int_0^\infty \frac{1}{2} W_\Sigma(f_s) e^{i[\omega_s + 2k_o \underset{\sim}{\alpha}_{o\perp} \cdot \bar{\underset{\sim}{v}}_{oD}]\tau} \\ \cdot \langle \delta(\underset{\sim}{\nu}_o - \underset{\sim}{F}_\Sigma(\alpha, f_s)/2\pi) \rangle_\alpha \, df_s, \end{aligned}\right\} \quad (7.9)$$

where $\underset{\sim}{\nu}_o$ is again given by (7.7). Now W_Σ is real-positive. [In fact, it may be obtained by the Wiener- Khintchine theorem ((3.42), [24]) applied to (7.5a) on setting $\underset{\sim}{\Delta r} = 0$ therein, viz.:

$$W_\Sigma = 2\mathcal{F}_\tau\{K_\Sigma\} = 2 \int_{-\infty}^{\infty} K_S(0,\tau) K_{N(0)}(0,\tau) F_2(0,\tau)_G e^{-i\omega\tau} \, d\tau, \quad (7.9a)$$

(or to (7.8) with $\underset{\sim}{\Delta r} = 0$), where $F_{2\text{-}G}$ is given by (6.4d,e).] Now $\underset{\sim}{F}_\Sigma \equiv \underset{\sim}{K}_\Sigma^{(\alpha)} = \hat{\underset{\sim}{i}}_\Sigma K_\Sigma^{(\alpha)}(f_s)$, and the precise form of $\underset{\sim}{K}_\Sigma^{(\alpha)}$ depends on the dispersion law appropriate to the ("product") wave surface, Σ, in question. Equation (7.9) is consistent with waves in the "forward" or wind-direction only, e.g., $-\pi/2 \leq \alpha - \Phi_w \leq \pi/2$, cf. Fig. 7.1 and (7.9c). Also, we have $W_\Sigma(f_s) = W_\Sigma(-f_s)$ formally, although physically only $f_s > 0$- represents real wave frequencies.

Next, it can be shown [27] that

$$\left.\begin{aligned} \delta(\underset{\sim}{\nu} - \underset{\sim}{F}_\Sigma(\alpha, f_s)/2\pi) = \delta\left(\nu_x - \frac{K_{\Sigma x}}{2\pi}\cos\alpha\right)\left(\nu_y - \frac{K_{\Sigma y}}{2\pi}\sin\alpha\right) \\ = \frac{1}{\nu}\,\delta(\nu - K_\Sigma(f_s)/2\pi)\,\delta(\phi_\nu - \alpha) \end{aligned}\right\} = \int_{(\alpha)} e^{2\pi i \underset{\sim}{\rho} \cdot (\underset{\sim}{\nu} - \underset{\sim}{K}_\Sigma/2\pi)} \, \underset{\sim}{d\rho} \quad (7.10)$$

in both rectangular and polar coordinates [$\nu = |\underset{\sim}{\nu}|$, with $\underset{\sim}{\nu} = (\nu, \phi_\nu)$]. In addition, we have directly the general relation

$$\delta(\nu - K_\Sigma(f_s)/2\pi) = \delta(f_s - G_\Sigma(\nu)) \left| \frac{df_s}{d\nu} \right| ; \quad G_\Sigma(\nu) = G_\Sigma\left(\frac{K_s}{2\pi}\right) = f_s, \quad (7.11)$$

so that the polar form of (7.10) becomes directly

$$\boxed{\delta(\underset{\sim}{\nu} - \underset{\sim}{F}_\Sigma/2\pi) = \frac{1}{\nu}\left|\frac{df_s}{d\nu}\right| \delta(f_s - G_\Sigma(\nu))\ \delta(\phi_\nu - \alpha),} \quad \text{and} \quad \left|\frac{df_s}{d\nu}\right| = \left|\frac{dG_s}{d\nu}\right|. \tag{7.12}$$

The dispersion law here is formally expressed by (7.11): $G(\nu) = f_s$, in this inverse form.

Applying (7.12) to (7.9) gives at once

$$\boxed{\Phi_\Sigma(\nu_o,\tau) = \left\langle e^{2ik_o \underset{\sim}{\alpha}_{o\perp} \cdot \Delta\underset{\sim}{v}_D \tau}\right\rangle_D \cdot \frac{1}{2\nu_o}\left|\frac{dG}{d\nu}\right|_{\nu_o} \langle\delta(\phi_{\nu_o} - \alpha)\rangle_\alpha W_\Sigma(G_\Sigma(\nu_o)) \cdot e^{i[2\pi G_\Sigma(\nu_o) + 2k_o \underset{\sim}{\alpha}_{o\perp} \cdot \underset{\sim}{\bar{v}}_{oD}]\tau}.} \tag{7.13}$$

In addition, we have

$$\langle\delta(\phi_{\nu_o} - \alpha)\rangle_\alpha = \int_{(\alpha)} w_1(\alpha)\delta(\phi_{\nu_o} - \alpha)\, d\alpha = w_1(\phi_{\nu_o})_\alpha;\ -\pi/2 \leqslant \alpha - \Phi_w \leqslant \pi/2, \tag{7.14}$$

where $w_1(\ )_\alpha$ is the pdf of "wave" directions, as noted above and elsewhere, cf. Eq. (7.4) et seq. Our general result (7.13) shows at once the contributions to the (angular) doppler shift, e.g.,

$$\boxed{\delta\omega_o \equiv 2\pi G_\Sigma(\nu_o) + 2k_o \underset{\sim}{\alpha}_{o\perp} \cdot \underset{\sim}{\bar{v}}_{oD}}\ . \tag{7.15}$$

The first term of (7.15) is the Bragg scatter component and the second term embodies that due to the fluid flow. The averaged term , $\langle\ \rangle_D$, in (7.13) contributes to the doppler spread [cf. remarks in Sec. 7.3 ff.].

7.2 Doppler Shift II: Various Dispersion Laws

To obtain a specific doppler shift we must, of course, know the dispersion law of the wave surface Σ. As an example, we consider the following wave types:

I. Gravity-Capillary Waves:

$$\omega_s = \sqrt{gK_s + \frac{\mathcal{T}}{\rho_w} K_s^3}\ , \quad \text{or } G(\nu) = \sqrt{\frac{g\nu}{2\pi} + 2\pi\nu^3 \frac{\mathcal{T}}{\rho_w}} = f_s; \tag{7.16a}$$

with $\mathcal{T}$ the surface tension parameter = 74 dynes cm^{-1}, p. 176 of [26]; ρ_w = density of water (g/cm^3).

Ia. Gravity Waves (primarily):

$$\begin{cases} \omega_s^2 = gK_s, \quad \therefore K_s = \omega_s^2/g; \ \nu \equiv \dfrac{K_s}{2\pi} = \omega_s^2 / 2\pi g, \ \text{or} & (7.16b) \\ f_s = G(\nu) = \sqrt{g\nu/2\pi}\ . & (7.16c) \end{cases}$$

Ib. Capillary Waves (primarily):

$$\omega_s = (\mathcal{T}/\rho_w)K_s^{3/2}, \quad \text{or} \quad G(\nu) = \sqrt{2\pi\nu^3\mathcal{T}/\rho_w} = f_s\ . \tag{7.16d}$$

II. Soliton Ensemble (Non-dispersive):

$$f_s = c_s\nu = c_sK_s/2\pi; \quad G(\nu) = c_s\nu = f_s. \tag{7.16e}$$

From (7.16) we readily obtain the desired inverses $f_s = G(\nu)$, viz.:

Ia. Gravity Waves:

$$\delta(\nu - af_s^2) = \frac{1}{2\sqrt{a\nu}}\,\delta(f_s - \sqrt{\nu/a}) = \frac{1}{2\sqrt{2\pi\nu/g}}\,\delta(f_s - \sqrt{g\nu/2\pi})\,; \tag{7.17a}$$

Ib. Capillary Waves:

$$\delta(\nu - bf_s^{2/3}) = \frac{3\sqrt{\nu}}{2b^{3/2}}\,\delta(f_s - (\nu/b)^{3/2}); \quad b = \rho_\omega/\mathcal{T}\cdot(2\pi)^{1/3}; \tag{7.17b}$$

II. Soliton Ensemble:

$$\boxed{\delta(\nu - af_s) = a^{-1}d(f_s - \nu/a) = c_s\delta(f_s - c_s\nu), \ \text{or} \ G(\nu) = c_s\nu = f_s,} \tag{7.17c}$$

which last we shall use for our scatter mechanism here, to determine the desired doppler shifts δf_o ($= \delta\omega_o/2\pi$), both for the soliton surface and the "classical" wave surface models I, Ia,b above.

7.3 Soliton Surface "Waves"

For (7.16), (7.17) to apply specifically here, i.e., for us to use these specific dispersion laws, we must, of course, have the corresponding wave surfaces. This means that in (7.5a) the wave surface Σ must refer either to models of the type I, or II above: this means, in turn, that $K_N(0)$, $F_{2\text{-}G}$ must be essentially independent of $\underset{\sim}{\Delta r}$, so that $K_S(\underset{\sim}{\Delta r},\tau)$ is the directional covariance of the particular surface, Σ, for which (7.16), (7.17) hold.

For the present soliton case we use (7.17c) in (7.13), along with (7.6), (7.8a), to write directly

$$M_{RT}^{(0)}(\tau|f_o) = B\Phi_\Sigma = D_o(\tau|\phi_{\nu_o},\nu_o=f_o\left|2\underset{\sim}{\alpha}_{o\perp}\right|/c_o)\; e^{\{i\omega_o[c_s|2\alpha_{o\perp}|/c_o+2\underset{\sim}{\alpha}_{o\perp}\cdot\underset{\sim}{\bar{v}}_{oD}/c_o]\tau\}}, \tag{7.18}$$

with $G(\nu_o) = c_s\nu_o$. [Here $D_o(\tau|\underset{\sim}{\nu}_o)$ is given explicitly by all factors in (7.13) not containing the doppler shift term.] The doppler shift contributions are seen at once to be the coefficient of τ in (the exponent of) (7.18), as we shall show in more detail below. The quantity D_o is real and positive, vanishing according to (7.14) outside the allowed interval for $\alpha\text{-}\Phi_w$: this corresponds to soliton "waves" moving downwind only, and not against the wind direction.

Our next step is to apply (7.18) for $M_{RT}^{(0)}(\tau)$ to (6.2), observing that except for the exponential term in (7.18) $M_{RT}^{(0)}(\tau|f_o)$ is even in τ. Since $K_o(\tau)_{in} = K_o(-\tau)_{in}$, cf. (6.26), we can write the intensity spectrum (6.3) of the (incoherent) scatter return as

$$W_{X-\langle X\rangle}(f) = k^2G^{(1)}\int_{-\infty}^{\infty} K_o(\tau)_{in}D_o(\tau|\phi_{\nu_o},\nu_o)\cos(\omega-\hat{b}_o)\tau\, d\tau, \tag{7.19}$$

where now

$$\hat{b}_o = \omega_o(1 - |2\underset{\sim}{\alpha}_{o\perp}|c_s/c_o - 2\underset{\sim}{\alpha}_{o\perp}\cdot\underset{\sim}{\bar{v}}_{oD}/c_o) \equiv \omega_o + \delta\omega_o. \tag{7.20}$$

[We have chosen the signs in the frequency dependent terms in (7.20) to conform to the geometry of Fig. 7.1: the scattering region is downwind from the receiver. Thus, for <u>downwind</u> here, we have $0 < \Phi_w < \pi$; for <u>upwind</u>, we have $\pi < \Phi_w < 2\pi$. From (7.20) it is immediately evident that the desired (general) doppler shift δf_o is

$$\boxed{\delta f_o = \frac{\delta\omega_o}{2\pi} = -\,|2\underset{\sim}{\alpha}_{o\perp}|\,c_s f_o/c_o - 2\underset{\sim}{\alpha}_{o\perp}\cdot\bar{\underset{\sim}{v}}_{oD} f_o/c_o.} \tag{7.21}$$

Applying (7.4a) to (7.2) and using (7.7) gives explicitly, for the present backscatter geometry ($\phi_{oT} = \pi/2$):

$$\boxed{\delta f_o = -\frac{2\sin\theta_{oT}}{\lambda_o}\,[c_s + \bar{v}_c \sin\phi_c + \bar{v}_d \sin\Phi_w], \quad \text{or}} \tag{7.22a}$$

$$\boxed{= -2f_o \sin\theta_{oT}\,[\frac{c_s}{c_o} + \frac{\bar{v}_c}{c_o}\sin\phi_c + \frac{\bar{v}_d}{c_o}\sin\Phi_w\,]}\,, \tag{7.22b}$$

which is the relation needed in Sec. 3, earlier. Note that for the deterministic components of the moving <u>fluid</u>, i.e., the deep current and drift layer, the azimuthal angles of observation (ϕ_c, Φ_w) appear explicitly, while for the <u>random</u> moving <u>interface</u>, determined by the soliton ensemble, it is the magnitude of the solitons' speed (on the drift layer) which is important, without azimuthal angles. [The azimuthal angle of viewing, ϕ_ν here, influences the observed spectral intensity, through $w_1(\phi_\nu)$ in D_o, cf. (7.18), but not the doppler shift component.]

In addition, from (7.18) and (7.19) it is at once evident that when $\underset{\sim}{\Delta v}_D = 0$, here, so that D_o is independent of τ, then D_o is proportional to the "spectral weight" or line intensity of the Bragg scatter component of the moving surface, selected by our choice of illuminating frequency f_o. Because of the planar character of the dispersion relations (7.18), (7.17) for these small-amplitude surface "waves," the resulting frequency spectrum is a <u>line spectrum</u>. Thus, letting the illuminating waveform be purely sinusoidal, so that $K_o(\tau)_{in} = (A_o^2/2)$, cf. (6.2b), we see that (7.19) becomes

$$W_{X-\langle X\rangle}(f)\Big|_{cw} = D_o(\phi_\nu,\nu_o)k_o^2 G^{(1)}\,\frac{A_o^2}{2}\int_{-\infty}^{\infty}\cos(\omega-\hat{b}_o)\tau\,d\tau$$

$$= k_o^2\,\frac{A_o^2}{2}\,G^{(1)}D_o(\phi_\nu,\nu_o)\delta(f-[f_o+\delta f_o]);\ \nu_o = |2\underset{\sim}{\alpha}_{o\perp}|f_o/c_o, \tag{7.23}$$

as remarked above. For (narrow band) but not purely sinusoidal illuminations (7.19) reduces directly to

$$W_{X-\langle X\rangle}(f-[f_o+\delta f_o]) = k_o^2 G^{(1)} D_o(\phi_\nu,\nu_o)\, w_{in}[f-(f_o+\delta f_o)], \tag{7.23a}$$

which has the spectral shape of the narrow-band injected signal, cf. Fig. 11, [2].

Actually, as we shall see explicitly later [cf. Secs. 8, 10], the line spectrum (7.23) is somewhat broadened, because of the "doppler smear" produced by the random variability of the various fluid and interface velocities, e.g., $\underset{\sim}{\Delta v}_d \neq 0$, (7.2), etc., and the random "tilting" of the large-scale surface, embodied in $K_N(0)$, cf. ③, Eq. (6.3). The resulting doppler spread, ΔF, accompanying the doppler shift δf_o, cf. (7.22) here, may be calculated from $D_o(\phi_\nu,\nu_o)$ by a perturbation, allowing $\nu_o \to \nu_o + \Delta\nu_o$ ($\sim \Delta F/c_o$) therein, or by a direct calculation of (7.5) in (6.2). In either case we need the specific structure of the covariance functions involved, viz. (7.5a). These we obtain in Section 9 ff.

7.4. The "Classical" Wave Surface

Using (7.17a) in (7.12) and applying it to (7.13) gives directly the wave number-time intensity spectrum for the purely gravity-wave surface ($\lambda_o > 2$ cm). We have

$$\Phi_G(\nu_o,\tau)_{grav.} = \frac{1}{4}\sqrt{\frac{g}{2\pi\nu_o}}\, F_1(2ik_o \underset{\sim}{\alpha}_{o\perp}\cdot\underset{\sim}{\hat{i}}_D\tau)_D\; W_G(\sqrt{g\nu_o/2\pi})\langle\delta(\phi_\nu-\alpha)\rangle_\alpha \cdot e^{i(2\pi\sqrt{g\nu_o/2\pi} + 2k_o\underset{\sim}{\alpha}_o\cdot\underset{\sim}{\bar{v}}_{oD})\tau}, \tag{7.24}$$

where $F_{1\text{-}D}$ is the average $\langle\ \rangle_D$, cf. (7.13a). Using (7.14) we readily obtain the counterpart of (7.18), viz.:

$$M_{RT}^{(0)}(\tau|f_o)_{grav.} = B\Phi_{\Sigma\text{-grav.}} = D_o(\tau|\phi_\nu;\nu_o)_{grav.}\exp\left\{i\left[\frac{\omega_o}{c_o}2\underset{\sim}{\alpha}_{o\perp}\cdot\underset{\sim}{\bar{v}}_{oD} + \sqrt{\frac{\bar{\omega}_o}{c_o}g\left|2\underset{\sim}{\alpha}_{o\perp}\right|}\right]\right\} \tag{7.25}$$

where now the weighting D_o is explicitly

$$D_o(\tau|\phi_\nu;\underset{\sim}{\nu}_o)_{grav.} = \frac{B}{4}\sqrt{\frac{g}{2\pi\nu_o}}\,F_1(2ik_o\underset{\sim}{\alpha}_{o\perp}\cdot\hat{\underset{\sim}{i}}_D\tau)_D\,W_\Sigma(\sqrt{g\nu_o/2\pi})w_1(\phi_\nu) \tag{7.25a}$$

analogous to (7.18).

The desired doppler shift is obtained as before, cf. (7.19)-(7.22), and is at once seen to be, generally,

$$\delta f_o = -[\sqrt{g|2\underset{\sim}{\alpha}_{o\perp}|/2\pi\lambda_o} + 2\underset{\sim}{\alpha}_{o\perp}\cdot\underset{\sim}{\bar{v}}_{oD}/\lambda_o], \tag{7.26a}$$

and specifically here for backscatter (with $\phi_{oT} = \pi/2$)

$$\boxed{\delta f_o = -\left\{\sqrt{\frac{g\,\sin\theta_{oT}}{\pi\lambda_o}} + \frac{2\sin\theta_{oT}}{\lambda_o}\,[\bar{v}_c\sin\phi_c + \bar{v}_d\,\sin\Phi_w]\right\},} \tag{7.26b}$$

including the surface drift.

For the complete gravity-capillary wave surface we use (7.16a) in (7.12) to get

$$\delta(\underset{\sim}{\nu}-\underset{\sim}{F}/2\pi) = \frac{g+3K_o^2\beta}{2\sqrt{gK_o+\beta K_o^3}}\,\delta\left(f_s - \sqrt{g\nu_o/2\pi + \beta\nu_o^3 2\pi}\right)\delta(\phi_\nu-\alpha);\quad \beta \equiv \mathcal{J}/\rho_w;\quad K_o = 2\pi\nu_o. \tag{7.27}$$

Accordingly, we replace the first term of (7.26b) by

$$\sqrt{\frac{g\,\sin\theta_{oT}}{\pi\lambda_o} + 16\pi\beta\,\frac{\sin^3\theta_{oT}}{\lambda_o^3}}\quad, \tag{7.28}$$

for the complete effect on δf_o now. However, for our present applications, (7.26b) is quite sufficient, since $\lambda_o \geqslant 7.5$ cm here, and the capillary régime does not dominate until about $\lambda_o \leqslant (\frac{1}{2} - 1)$ cm, cf. p. 178 of [26].

8. Doppler Spread, I: $M_{RT}^{(0)}$

To obtain the doppler spread, ΔF, we need the explicit structure of ①, ③, and ④ in (6.3). [It turns out here that we do not need the explicit covariance, $K_S(\underset{\sim}{\Delta r},\tau)$, of the soliton ensemble for this purpose.

Of course, K_S is required if we desire the (intensity) spectrum of the scatter return itself, and it is needed for the backscatter intensity, cf. Sec. 2. See Eqs. 8.9 ff.] Accordingly, we begin with:

8.1 "Flow" Spread

Here we need to evaluate

$$F_1(2ik_o\underset{\sim}{\alpha}_{o\perp}\cdot\hat{\underset{\sim}{i}}_D\tau)_D \equiv \left\langle e^{i2k_o\underset{\sim}{\alpha}_{o\perp}\cdot\underset{\sim}{\Delta v}_D\tau}\right\rangle_D \tag{8.1}$$

for the fluctuations, $\underset{\sim}{\Delta v}_D$, in the deep current and surface drift velocities, cf. (7.1), (7.2). Making the usual (reasonable) gaussian assumption for each independent component of $\underset{\sim}{\Delta v}_D$, writing

$$\Delta\hat{v}_c \equiv (2\underset{\sim}{\alpha}_{o\perp}\cdot\hat{\underset{\sim}{i}}_c)\Delta v_c; \quad \Delta\hat{v}_d \equiv (2\underset{\sim}{\alpha}_{o\perp}\cdot\hat{\underset{\sim}{i}}_d)\Delta v_d, \tag{8.2}$$

gives directly

$$\left\langle e^{i\omega_o\tau[2\underset{\sim}{\alpha}_{o\perp}\cdot\underset{\sim}{\Delta v}_D/c_o]}\right\rangle_D = \left\langle e^{i\omega_o\tau\Delta\hat{v}_c/c_o}\right\rangle\left\langle e^{i\omega_o\tau\Delta\hat{v}_d/c_o}\right\rangle$$

$$\therefore \quad \boxed{F_1 = e^{-\omega_o^2\tau^2\sigma_\beta^2/2}} \; . \tag{8.3}$$

Here the variance σ_β^2 is specifically

$$\sigma_\beta^2 \equiv (2\underset{\sim}{\alpha}_{o\perp}\cdot\hat{\underset{\sim}{i}}_c/c_o)^2\sigma_c^2 + (2\underset{\sim}{\alpha}_{o\perp}\cdot\hat{\underset{\sim}{i}}_d/c_o)^2\sigma_d^2; \quad \sigma_c^2 \equiv \overline{\Delta v_g^2}; \quad \sigma_d^2 \equiv \overline{\Delta v_d^2} \; . \tag{8.4}$$

These random fluctuations produce, as expected, cf. (8.3), a random phase modulation, which depends on the input signal frequency f_o.

In our present model of the soliton surface ensemble we postulate that the variance in the soliton surface speed c_S is essentially negligible, so that $\overline{\Delta c_S^2} \doteq 0$, e.g., $\hat{\sigma}_S^2 \equiv \overline{\Delta c_S^2} \doteq 0$: there is negligible doppler spreading due to variations in the speed of travel of the numbers of the soliton ensemble generated by "wind-wave-wind" interactions on the large-scale surface (as described in [3] and [4]). The major variations appear in the size of the individual solitons which comprise the

hydraulic impulses produced on the large-scale surface, cf. Fig. 3.1(d), [4], for example. [See Sec. 9 for additional remarks.]

8.2 Spreading Due to the Large-Scale Wave Surface Motion, I. Random Phase Modulation

Next, we consider the effect of the (primarily here) temporal variations in the large-scale surface, primarily the gravity-wave component (G), as exhibited by ④, namely $F_{2\text{-}G}$, Eq. (6.4d,e). These also produce a random phase modulation, dependent on the illuminating frequency (f_o).

Using (6.4e) and the basic relation (7.8) allows us to write for the directional covariance of the large-scale wave surface (G) here

$$\sigma_G^2 \rho_G(\underset{\sim}{\Delta r},\tau) = \int_0^\infty W_G(f_s)\langle \cos(\omega_s \tau - \underset{\sim}{K}_G \cdot \underset{\sim}{\Delta r})\rangle_\alpha \, df_s, \quad \tau = t_2 - t_1, \quad \sigma_G^2 = \overline{\zeta_G^2} \tag{8.5}$$

with $\underset{\sim}{K}_G \cdot \underset{\sim}{\Delta r} = K_G \Delta r \cos(\Delta\phi - \alpha)$, ($\underset{\sim}{\Delta r} \equiv \underset{\sim}{r}_2 - \underset{\sim}{r}_1$, $\Delta r = |\underset{\sim}{\Delta r}|$; $\Delta\phi = \phi_2 - \phi_1$, etc.), and K_G ($=K_s$) of (7.16), in the usual way. Here $W_G(f_s)$ is the "point"-intensity spectrum of the wave surface elevation $\zeta(\underset{\sim}{r},t)$. [The semi-empirical model we use here explicitly for W_G is the well-known Pierson-Moskowitz result [15], Eq. (1.1) above.]

For the large Rayleigh numbers involved in the present study we note that the principal contribution to the exponent of (6.4e) arises for small $\underset{\sim}{\Delta r}$ and τ. Consequently, we seek a Taylor's expansion of ρ_G about $\underset{\sim}{\Delta r} = 0$, $\tau = 0$, with W_G as yet unspecified. For a pdf of α of the form (7.4c) for the different wave directions, we readily find that the only non-vanishing terms in the expansion (through the second order) are such that

$$\sigma_G^2 \rho_G(\underset{\sim}{\Delta r},\tau) = 1 - \frac{1}{2!}\left\{ \sigma_x^2 (\Delta x)^2 + \sigma_y^2 (\Delta y)^2 + \frac{\tau^2 \sigma_{\dot\zeta}^2}{\sigma_G^2} - \tau \Delta x \sigma_{x\tau}^2 \right\} + O(\Delta x^3, \tau^3), \tag{8.6}$$

where specifically

$$\sigma_{x,y}^2 = \int_0^\infty K_G^2 \begin{pmatrix} \langle \cos^2\alpha \rangle \\ \langle \sin^2\alpha \rangle \end{pmatrix} W_G \, df_s = \overline{\zeta_{x,y}^2} \quad (>0); \tag{8.7a}$$

$$\sigma_{x\tau}^2 = \int_0^\infty \omega_s K_G \, \overline{\cos\alpha} \; W_G \, df_s \quad (>0); \tag{8.7b}$$

$$\sigma_{\dot\zeta}^2 = \int_0^\infty \omega_s^2 W_G \, df_s = \overline{\dot\zeta^2} \quad (> 0). \tag{8.7c}$$

Applying (8.6) to (6.4e) allows us to write now

$$\boxed{\begin{aligned} F_{2\text{-}G} &= e^{-(2\sigma_G k_o \alpha_{oz})^2 (1-\rho_G)} \\ &\doteq e^{-\frac{1}{2}(2\alpha_{oz}k_o)^2[\sigma_x^2\Delta x^2+\sigma_y^2\Delta y^2+\tau^2\sigma_{\dot\zeta}^2]+\frac{1}{2}(2\alpha_{oz}k_o)^2\tau\Delta x\sigma_{x\tau}^2} . \end{aligned}} \tag{8.8}$$

At this stage we use the P-M spectrum (1.1) and make a variety of approximations, to simplify (8.8) vis-à-vis the small-scale (soliton) surface component. Let us consider first $\sigma_{x\tau}^2$, (8.7b). We have, since $K_G = \omega_s^2/g$, from (7.16b),

$$\sigma_{x\tau}^2\Big|_{PM} = \int_0^\infty \omega_s \left(\frac{\omega_s^2}{g}\right) \overline{\cos\alpha} \cdot \left\{ Cg^2\omega_s^{-5} e^{-ag^4/\omega_s^4 \overline{U_a}^4} \right\} df_s, \quad [a = 0.74,\ C = 8.10\cdot 10^{-3}] \tag{8.9a}$$

$$= \frac{C_g \overline{\cos\alpha}}{2\pi} \int_0^\infty x^{-2} e^{-B/x^4} dx = \frac{Cg\ \overline{\cos\alpha}}{8\pi B^{1/4}} \int_0^\infty y^{-3/4} e^{-y} dy; \quad B \equiv ag^4/\overline{U_a}^4$$

$$\therefore \boxed{G_{x\tau}^2\Big|_{PM} = \frac{C\overline{U_a}\,\Gamma(1/4)\ \overline{\cos\alpha}}{8\pi a^{1/4}}} . \tag{8.9b}$$

Next, we use $\Gamma(1/4) = 4\Gamma(5/4) = 4(0.906) = 3.624$; $a^{1/4} = (0.74)^{1/4} = 0.93$; and a $\cos^2\alpha$ law, viz. $w_1(\alpha) = \frac{2}{\pi}\cos^2\alpha$ from (7.4c), $-\pi/2 \leqslant \alpha \leqslant \pi/2$, to get $\overline{\cos\alpha} = 3/\pi$, so that (8.9b) becomes, at $\overline{U_a} = 10$ m/sec,

$$\sigma_{x\tau}^2\Big|_{PM} = \frac{3}{8\pi^2}(8.10\ 10^{-3})\ \frac{10(3.624)}{0.93} = \boxed{1.20\cdot 10^{-2}\ (\text{msec})^{-1}};\ \overline{U_a} = 10\ \text{m/sec} . \tag{8.9c}$$

Also, from (2.5), the Cox and Munk's relation [17], we obtain (as a result of the $w_1(\alpha) = (2/\pi)\cos^2\alpha$ assumption)

$$\boxed{\sigma_x^2 = 3\sigma_y^2 = 5.42\cdot 10^{-2}}\ ;\ \overline{U_a} = 10\ \text{m/sec}. \tag{8.10}$$

In addition, for the strictest case here at f_o = 20 kHz, we have k_o = 83.78 rad m^{-1}; $2\alpha_{oz} = 2\cos\theta_{oT} = 2\cos 81° = 0.313$, so that

$$\boxed{(2\alpha_{oz}k_o)^2 = [(0.313)\cdot 83.78]^2 = [26.21]^2 = 6.87\cdot 10^2\ (m^{-2}).} \tag{8.11}$$

At this point we use the (normalized) space- and time-covariances of the soliton ensemble to obtain their correlation lengths and times, from (9.7), (9.13), namely.

$$x_{-1}K_1(x_{-1}) = e^{-1}; \qquad x_{-1} = \frac{2\Delta r_c}{\sigma_h}; \qquad x_{-1} = \frac{2c_s\tau_c}{\sigma_h}. \tag{8.12}$$

From Watson, p. 737 [30], we see that x_{-1} = 1.65, so that using σ_h = 5.0 cm, from the backscatter cross-sectional and doppler shift data of Roderick, cf. Fig. 2.2, 3.1, appropriate here, we get for the correlation lengths and times of the surface-riding soliton ensemble

$$\Delta r_c = \frac{1.65}{2}\sigma_h = 4.13\cdot 10^{-2}\ \text{m}; \quad \tau_c = \frac{1.65}{2}\sigma_h/c_s = 0.28\ \text{sec}, \tag{8.13}$$

where we have used c_s = 15 cm/sec, in line with Table 3.1.

There remains the calculation of $\sigma_{\dot\zeta}^2$, (8.7c), for the PM spectrum. We get

$$\boxed{\sigma_{\dot\zeta}^2 = C\sqrt{\pi}\,\overline{U_a}^2/8a^{1/2} = 2.09\cdot 10^{-3}\,\overline{U_a}^2 = 0.209}, \quad \overline{U_a} = 10\ \text{m/sec}. \tag{8.14}$$

Let us now use (8.13), $\Delta r = \sqrt{\Delta x^2+\Delta y^2} = \Delta r_c$, (8.10) and (8.11) to compute the purely spatial part of the exponent of (8.8). We get

$$\tfrac{1}{2}(2\alpha_{oz}k_o)^2(\sigma_x^2\Delta x_c^2 + \sigma_y^2\Delta y_c^2) < \tfrac{1}{2}(2\alpha_{oz}k_o)^2\sigma_x^2\Delta r_c^2 = \tfrac{1}{2}(6.87\cdot 10^2)(5.42)10^{-2}(4.13\ 10^{-2})^2$$
$$= \boxed{3.17\cdot 10^{-2}}. \tag{8.15}$$

Similarly, we use $\tau \to \tau_c$, $\Delta x \to \Delta r_c$, (8.9c), (8.11) to get

$$\frac{1}{2}(2\alpha_{oz}k_o)^2\tau\Delta x\sigma_{x\tau}^2 < \frac{1}{2}(2\alpha_{oz}k_o)^2\tau\Delta r_c\sigma_{x\tau}^2 = \frac{1}{2}(6.87\ 10^2)(4.13\cdot 10^{-2})(1.20\cdot 10^{-2})\tau$$

$$= \boxed{0.170\ \tau}\ , \qquad (8.16)$$

and

$$\frac{1}{2}(2\alpha_{oz}k_o)^2\sigma_{\dot{\zeta}}^2\tau^2 = \frac{1}{2}(6.87\cdot 10^2)(0.209)\tau^2 = \boxed{71.8\tau^2}\ . \qquad (8.17)$$

For $\tau = O(\tau_c) = 0.3$ secs, cf. (8.13), clearly

$$0.170\tau_c = 0.051 << 71.8(0.3)^2 = \boxed{6.46}\ , \qquad (8.18)$$

so that we can very safely neglect the last term ($\sim \sigma_{x\tau}^2$) in the exponent of (8.8). In addition, from (8.15) in (8.8) we see that the spatial contribution is negligible, so that we obtain the much simpler, approximate form for $F_{2\text{-}G}$:

$$\boxed{F_{2\text{-}G} \doteq e^{-\omega_o^2\tau^2 R_{\dot{\zeta}}/2}\ ; \qquad R_{\dot{\zeta}} \equiv (2\alpha_{oz}\sigma_{\dot{\zeta}}/c_o)^2}\ . \qquad (8.19)$$

The result is thus purely a doppler spread due to the random phase modulation of the incident signal ($\sim f_o$), produced by the movement of the local large-scale surface (G), as we might expect. For frequencies less than $f_o = 20$ kHz, the above approximations are even better.

8.3 Spreading Due to the Local "Tilting" of the Small-Scale Surface Component, II. Random Amplitude Modulation

The third element producing doppler spread is the random amplitude modulation generated by the time-varying slope of the large-scale surface ③, on which the small-scale, soliton ensemble rides. Because of the assumed local homogeneity (and stationarity) of the large-scale surface, $\zeta(\underset{\sim}{r},t)_G$, the statistics of these slope variations are also essentially independent of position for the small $\Delta r = \Delta r_c$ regions involved vis-à-vis the soliton ensemble.

The evaluation of $K_{N(0)}(\underset{\sim}{\Delta r},\tau)$ in (6.3) proceeds from Eq. (7.28), [1], where we have explicitly

$$\boxed{K_{N(0)}(\underset{\sim}{\Delta r},\tau) \equiv \langle\{(\hat{\underset{\sim}{n}}_1\cdot 2\underset{\sim}{\alpha}_o/n_{z1})(\hat{\underset{\sim}{n}}_1\cdot 2\underset{\sim}{\alpha}_o)\}\{(\hat{\underset{\sim}{n}}_2\cdot 2\underset{\sim}{\alpha}_o/n_{z2})(\hat{\underset{\sim}{n}}_2\cdot 2\underset{\sim}{\alpha}_o)\}\rangle_G} \quad , \tag{8.20}$$

where, as before (cf. (2.2a,b), [1]),

$$\hat{\underset{\sim}{n}}_G = (\hat{\underset{\sim}{i}}_x\zeta_x + \hat{\underset{\sim}{i}}_y\zeta_y - \hat{\underset{\sim}{i}}_z)\Big/(1+\zeta_x^2+\zeta_y^2)^{\frac{1}{2}} \; (\doteq \hat{\underset{\sim}{n}}_g); \quad n_z \equiv (1+\zeta_x^2+\zeta_y^2)^{-\frac{1}{2}} \; ; \tag{8.20a}$$

$$\therefore \; \hat{\underset{\sim}{n}} = (\hat{\underset{\sim}{i}}_x\zeta_x + \hat{\underset{\sim}{i}}_y\zeta_y - \hat{\underset{\sim}{i}}_z)n_z. \tag{8.20b}$$

For the small slopes encountered here ($\sigma_x^2 \sim \sigma_y^2 \sim 5\cdot 10^{-2}$, cf. (8.10)), we can drop the denominators ($\zeta_x^2 \to \overline{\zeta_x^2}$, etc.) $\ll 1$, on the average, and so write (8.20) approximately as

$$K_{N(0)} \doteq \langle(\hat{\underset{\sim}{n}}_1\cdot 2\underset{\sim}{\alpha}_o/n_{z1})^2(\hat{\underset{\sim}{n}}_2\cdot 2\underset{\sim}{\alpha}_o/n_{z2})^2\rangle_G. \tag{8.21}$$

Next, we use the following reasonable conditions and assumptions further to simplify (8.21), viz.:

(i). the pdf's of ζ_x, ζ_y are symmetrical in $-\infty < x,y < \infty$: all odd moments vanish; (8.22a)

(ii). $\overline{\zeta_x} = \overline{\zeta_y} = 0$; $\overline{\zeta_{x1}\zeta_{y2}} = -\overline{\zeta_{x2}\zeta_{y1}} \doteq \langle(\zeta_{x1}\zeta_{y1})(\zeta_{x2}\zeta_{y2})\rangle \doteq 0.$ (8.22b)

(Here 1 refers to t_1, 2 to t_2, $\Delta r \doteq 0$ on the soliton scale.) Expanding (8.21), subject to (8.22), and retaining (even) terms of order no higher than the quadratic (because of the small-slope condition, (8.10), etc.), we get, for our present geometry ($\phi_{oT} = \pi/2$), cf. (2.4) and Fig. 2.1 (and the assumption of isotropy: $\sigma_x^2 = \sigma_y^2$, etc.)

$$K_{N(0)}\Big|_{\phi_{oT}=\pi/2} \doteq 16\left\{\rho^{(2)}_{x=y}\sin^4\theta_{oT} + 2\sigma_x^2(2+\rho^{(1)}_{x=y})\sin^2\theta_{oT}\cos^2\theta_{oT} + \cos^4\theta_{oT}\right\}_G, \tag{8.23}$$

$\sigma_x^2 = \sigma_y^2 = \sigma_{x=y}^2$. Under the further reasonable assumption that ζ_x, ζ_y are normally distributed (since ζ_G is normal), we have

$$\rho^{(2)}_{x=y}(\tau) = \overline{\zeta^2_{x1}\zeta^2_{x2}} \,/\, \overline{\zeta^2_x}^2 = (2\rho^{(1)2}_{x=y} + 1); \quad \rho^{(1)}_{x=y} = \overline{\zeta_{x1}\zeta_{x2}} \,. \tag{8.23a}$$

Then, $K_{N(0)}$, (8.23), becomes

$$K_{N(0)}(\underset{\sim}{\Delta r},\tau) = K_{N(0)}(\tau) \doteq$$

$$\doteq 16\{(2\rho^{(1)2}_{x=y}+1)\sigma_x^4\sin^4\theta_{oT} + 2(2+\rho^{(1)}_{x=y})\sigma_x^2\sin^2\theta_{oT}\cos^2\theta_{oT} + \cos^4\theta_{oT}\}, \tag{8.24}$$

which reduces, as expected, to (2.4) when $\tau = 0$, $\rho^{(1)}_{x=y}(0) = 1$.

Our next step is to consider the expansion of $\rho^{(1)}_{x=y}(\tau)$ about $\tau = 0$, since it is only for small values of τ that $\rho^{(1)}_{x=y}$ makes a significant contribution. We have from (8.5)

$$\rho^{(1)}_{x=y}(\Delta r,\tau)_G = -\int_0^\infty K_G^2 \,\langle(\cos^2\alpha - \sin^2\alpha)\cos(\omega_s\tau - \underset{\sim}{K}_G\cdot\underset{\sim}{\Delta r})\rangle_\alpha \; W_G \; df_s \tag{8.25a}$$

$$\therefore \quad \rho^{(1)}_{x=y}(0,0)_G = -\overline{(\cos^2\alpha - \sin^2\alpha)} \int_0^\infty \omega_s^2 K_G^2 \; W_G(f_s)df_s \quad (< \infty: \text{ physically}), \tag{8.25b}$$

so that

$$\boxed{\rho^{(1)}_{x=y}(0,\tau)_G \doteq 1 + \frac{\tau^2}{2!}\,\ddot{\rho}^{(1)}_{x=y}(0,0)_G = 1 - \frac{\tau^2}{2}\{-\ddot{\rho}^{(1)}_{x=y}\big|_G\} \equiv 1 - \tau^2\Gamma_G} \quad (> 0) \tag{8.26}$$

This defines Γ_G, namely,

$$\boxed{\Gamma_G = -\frac{\ddot{\rho}^{(1)}_{x,y}(0)_G}{2!} = \frac{\overline{\cos^2\alpha}}{2g^2}\int_0^\infty \omega_s^6 \; W_G(f_s)df_s \quad (> 0)} \tag{8.26a}$$

when (7.16b) is used.

If we use the P-M model (1.1) for W_G in (8.35b), we get, with the help of the dispersion relation (7.16b),

$$\ddot{\rho}^{(1)}_{x=y}\Big|_{G:PM} = -C\,\overline{\cos^2\alpha}\int_0^{\infty}\omega_s e^{-ag^4/\omega_s^4\overline{U_a}^4}\,df_s \to -\infty, \tag{8.27}$$

which is, of course, not physically valid, since at sufficiently high frequencies (ω_k) the wave spectrum must vanish, e.g.,

$$\ddot{\rho}^{(1)}_{x=y}\Big|_{G:PM} = -C\cos^2\alpha\int_0^{\omega_k}\omega_s e^{-ag^4/\omega_s^4\overline{U_a}^4}\,df_s > -\infty. \tag{8.27a}$$

(Rather than attempt to evaluate (8.27a), since ω_k is uncertain, we shall determine Γ_G, or R_G, (8.29b), instead, from the experimental measurements of doppler spread, cf. Sec. 4.1.

Using (8.26) in (8.24) allows us to write*

$$K_{N(0)}(\tau) \doteq 16\{(3-4\tau^2\Gamma_G)\sigma_x^4\sin^4\theta_{oT} + 2(3-\tfrac{\tau^2}{2}\Gamma_G)\sigma_x^2\sin^2\theta_{oT}\cos^2\theta_{oT} + \cos^4\theta_{oT}\}, \tag{8.28a}$$

which can be put in the form

$$K_{N(0)}(\tau) \doteq N_{GS}^{(0)}\left[1 - \Gamma_G\frac{\tau^2}{2}\left\{\frac{8\sigma_x^4\sin^4\theta_{oT} + 2\sigma_x^2\sin^2\theta_{oT}\cos^2\theta_{oT}}{3\sigma_x^4\sin^4\theta_{oT} + 6\sigma_x^2\sin^2\theta_{oT}\cos^2\theta_{oT} + \cos^4\theta_{oT}}\right\}\right], \tag{8.28b}$$

which, in turn, for small τ can be rewritten as

$$\boxed{K_{N(0)}(\tau)\Big|_{\phi_{oT}=\pi/2} \doteq N_{GS}^{(0)}(\underset{\sim}{\alpha}_o)e^{-R_G\tau^2/2}.} \tag{8.29a}$$

Here, specifically,

$$\boxed{R_G \equiv \Gamma_G\cdot\left[\frac{8\sigma_x^4\sin^4\theta_{oT} + 2\sigma_x^2\sin^2\theta_{oT}\cos^2\theta_{oT}}{3\sigma_x^4\sin^4\theta_{oT} + 6\sigma_x^2\sin^2\theta_{oT}\cos^2\theta_{oT} + \cos^4\theta_{oT}}\right],} \tag{8.29b}$$

---

*Since we are interested only in small τ, we write $\ddot{\rho}^{(1)2}_{x=y} = (1 + \tau^2\Gamma_G + \;\;)^2 \doteq 1 + 2\tau^2\Gamma_G$, dropping terms $o(\tau^4)$.

with Γ_G determined from (8.26a), or (8.27a), when possible. In any case, K_G can be found (as is done here) from experiment, by measuring the doppler spread at several different frequencies.

The important feature to note here, in (8.29a), is that the random "tilt" of the large-scale surface produces an amplitude modulation of the scattered signal, which is independent of signal frequency. It is this effect which accounts for (i) the much larger observed doppler spread, ΔF, and (ii) the essentially non-vanishing character of ΔF as signal frequency (f_o) is decreased, cf. Fig. 4.1.

9. A Concise Summary of Middleton's Soliton Surface-Component Model [3], [4]

As noted in Sec. 1 above, after the nonlinear wind-wave interactions have reached a point of sufficient development, the resulting surface distortions, riding on a thin wind-drift layer, which in turn lies upon the large-scale gravity-capillary component, represent ensembles of solitons, of varying magnitude and duration. These surface distortions are thus decomposible into a set of hydraulic bumps (solitons), as observed by Peterson [31] and others [3]; [4], Fig. 3.1, for example. The thin, wind-drift layer of effective thickness h_{eff}, provides the necessary channel for the soliton to be created and move upon. These solitons are then produced as the limiting solutions of the famous Korteweg-deVries (KdV) equation, expressed in normalized coordinates by a relation of the form

$$\zeta_{t'} - 6\zeta\zeta_t + \zeta_{x'x'x'} = 0, \tag{9.1}$$

where ζ is the surface displacement, cf. [10], pp. 463-468 and [11], Secs. 1.2, 5.3. Here the various solitons, or solitary, one-sided hydraulic "bumps," are propagated under conditions where the dispersive and nonlinear forces in the (thin layer) of the medium are essentially balanced, [10], [11], and dissipative mechanisms (e.g., viscosity) are very weak and ignorable. (Ultimately, the effects of surface tension must be included also. These appear as a negative component of the dispersive forces and reduce the coefficient of the dispersive term ($\sim\zeta_{x'x'x'}$) in the KdV equation. The effective drift layer is now the soliton surface.*)

---

*D. Middleton, "A Proposed Soliton Mechanism in Wind-Wave Surface Generation and Scattering," NUSC Tech. Doc., in prep., June, 1986.

The (denormalized) solution of (9.1) can be shown to have the form

$$\zeta(r,t) = 3v_o \operatorname{sech}^2\left\{\sqrt{\frac{v_o}{2\sigma}}\,[r-r_j-(\hat{c}_o+v_o)(t-t_j)]\right\}, \tag{9.2}$$

at some point where we are considering the typical member of the ensemble, initiated at (r_j,t_j). Here v_o is the excess speed due to nonlinear effects, and $c_s = \hat{c}_o + v_o$, where $\hat{c}_o = \sqrt{gh_{eff}}$. Thus, c_s is the constant speed of the soliton: solitons travel at constant speed and their propagation is non-dispersive, i.e., $c_s\nu = f_s$, cf. (7.17c), unlike gravity and capillary waves, which are, of course, dispersive, cf. (7.17a,b). Here $v_o = v_{oj}$, which depends on the decomposition of the surface into particular soliton members, each traveling at excess speed, v_{oj}, while $\sigma = h_{eff}^{5/2}\sqrt{g}/6$. It can be shown that (9.2) can be well-approximated by [3]

$$\boxed{\zeta(r-r_j,t-t_j) = \zeta_o(v_o)_j e^{-4|r-r_j-c_s(t-t_j)|^2/L_{oj}^2}} \quad ; \quad L_{oj} = 2_g^{1/4} h_{eff}^{5/4} \Big/ \sqrt{3v_{oj}}\,,$$

$$\zeta_{oj} = 2\sqrt{\frac{h_{eff}}{g}}\, v_{oj} \tag{9.3}$$

Here L_{oj} is the "wavelength" of the typical soliton, and may be regarded as a random quantity over the soliton ensemble $\{j\}$, in consequence primarily of the composite random surface displacements or distortions, riding on the drift layer and large-scale surface component (G): many different sizes ($\sim v_{oj}$) of soliton are required, to constitute the surface distortion at r. Since ζ is a limiting form of solution of the KdV equation (9.1), a condition for (one-sided) solitons to exist is that (for each j)

$$\zeta_o L_o^2 \Big/ h_{eff}^3 > 8, \text{ with } L_o = \lambda_o/2;\ \lambda_o = \text{"wavelength" between } e^{-4} \text{ points.} \tag{9.3a}$$

Otherwise (two-sided) cnoidal waves are generated ([10], Eq. 100, p. 466). The resulting soliton ensemble defining the incremental (i.e., small-scale) surface at r is then given by

$$\zeta_S(r,t)_J = \sum_j^J \zeta(r-r_j,t-t_j) = \sum_j^J \zeta_{oj}\, e^{-4|r-r_j-c_s(t-t_j)|^2/L_{oj}^2} \tag{9.4}$$

The soliton ensemble is then $\{\zeta_{SJ}\}$, over all allowed values of J.

A reasonable distribution of values of the L_{oj} is provided by the pdf

$$\boxed{w_1(L_o) = \sqrt{\frac{2}{\pi}}\,\frac{1}{\sigma_h}\,e^{-L_o^2/2\sigma_h^2}} \quad ; \quad \sigma_h^2 = \overline{L_o^2} \quad ; \quad (\overline{L_o} = \sqrt{\frac{2}{\pi}}\sigma_h). \tag{9.5}$$

Because of the many forces influencing the local surface at r a Central Limit Theorem argument may be invoked to suggest the half-gaussian pdf (9.5) (since $L_o \geq 0$). Moreover, this pdf favors solitons with lengths shorter than $(\overline{L_o^2})^{\frac{1}{2}}$ $(= \sigma_h)$, although comparatively large values of L_o $(> \sigma_h)$ are not improbable, and, indeed, are needed, to provide significant backscatter returns at the longer Bragg-scatter wavelengths ($\lambda_o/2 \sim 15$ cm, at $f_o = 5$ kHz; $\lambda_o/2 = 7.5$ cm, at $f_o = 10$ kHz), cf. Fig. 2.2. [Another, supporting feature of our choice of pdf (9.5) is the perhaps fortuitous fact that it leads to a wave number intensity spectrum, $W_2(\underset{\sim}{k},0)_S$, which is $O(k^{-4})$ as k becomes large, cf. Eq. 9.15 ff.]

An important characteristic of solitons is the unusual feature that they remain undistorted when interacting with one another [11]. This suggests that the soliton ensemble, a representation (J) of which is given by (9.4), may be described by a poisson process in time (at any point r): superposition does not change the individual "wave" forms. Accordingly, we can show quite readily [3] that the temporal covariance associated with 9.3 is given by

$$K_S(0,\tau) = \sigma_S^2 \left\langle \frac{L_o e^{-2\Delta y^2/L_o^2}}{\langle L_o \rangle} \right\rangle_{L_o}, \qquad \Delta y \equiv c_S \tau, \tag{9.6}$$

where

$$K_S(0,0) = \sigma_S^2 = \frac{\overline{n_o}}{2}\,\overline{\zeta_o^2}\,\sqrt{\frac{\pi}{2}}\,\overline{L_o} \tag{9.6a}$$

is the resulting mean intensity of (all) the soliton components at (r_j,t_j) $[(r_j,t_j)_J$ does not appear in (9.6) because of our assumption of stationarity and homogeneity]; $\overline{n_o}$ is the average number of solitons per unit length, traveling in the direction of the wind, i.e., downwind generally. Applying (9.5) gives, for the point-covariance (9.6),

$$\boxed{K_S(0,\tau) = \sigma_S^2 \left|\frac{2c_s\tau}{\sigma_h}\right| K_1\left(\left|\frac{2c_s\tau}{\sigma_h}\right|\right)} \quad ; \quad \sigma_h^2 = \overline{L_o^2} \tag{9.7}$$

(where K_1 is a modified Bessel function of the second kind; note that $\lim_{x\to 0} xK_1(x) = 1.$). Here $c_s \doteq c_o$, since $c_o \gg v_o$, cf. remarks (1.1), p. 54 ff.

The associated point-intensity spectrum $W_S(f_s)$ is now readily obtained from the Weiner-Khintchine theorem ([24], p. 143):

$$W_S(f_s) = 2\int_{-\infty}^{\infty} K_S(0,\tau)e^{-i\omega_s\tau}\,d\tau \tag{9.8a}$$

$$= \frac{2\sigma_h\sigma_S^2}{c_s}\int_0^{\infty} xK_1(x)\cos ax\,dx; \quad a \equiv \omega_s\sigma_h/2c_s \tag{9.8b}$$

$$\boxed{W_S(f_s) = \frac{\pi\sigma_h\sigma_S^2}{c_s}\cdot\frac{1}{\left[1+\left(\frac{\omega_s\sigma_h}{2c_s}\right)^2\right]^{3/2}}} \quad \doteq \left(\frac{\pi\sigma_h\sigma_S^2}{c_s}\,\frac{1}{\left[1+\left(\frac{K_S\sigma_h}{2}\right)^2\right]^{3/2}}\right), \tag{9.9}$$

since $\omega_s/c_s = K_S$, (7.17c), for these nondispersive solitons.

Next, we use the basic directional form [(7.8), or (8.5)], now for these nondispersive solitons, where $K_S = \omega_s/c_s$, cf. (7.17c). The result of applying (9.9) therein is, finally [3], the general directional covariance

$$\boxed{K_S(\underset{\sim}{\Delta r},\tau) = \sigma_S^2 \langle |\beta(\alpha)| K_1(|\beta(\alpha)|)\rangle_\alpha} \quad ; \quad \beta(\alpha) \equiv \frac{2}{\sigma_h}[c_s\tau - \Delta r\cos(\Delta\phi-\alpha)], \tag{9.10}$$

with $\Delta r = r_2 - r_1$, $\Delta\phi = \phi_2 - \phi_1$, as before, cf. (8.5), r in the (x,y)-plane, of course. In our present application we assume <u>semi-isotropy</u>, e.g., K_S is independent of direction (in the downwind régime), so that we have

$$\therefore \quad \Delta\phi = \alpha, \tag{9.11}$$

and consequently (9.10) reduces to our earlier result [3], [4]

$$\boxed{K_S(\Delta r,\tau)\Big|_{\text{semi-iso}} = \sigma_S^2 \left|\frac{c_s\tau-\Delta r}{\sigma_h/2}\right| K_1\left(\left|\frac{c_s\tau-\Delta r}{\sigma_h/2}\right|\right).} \tag{9.12}$$

This reduces at once to

$$K_S(\underset{\sim}{\Delta r},0)_{s\text{-}iso} = \sigma_S^2 \left|\frac{2\Delta r}{\sigma_h}\right| K_1\left(\left|\frac{2\Delta r}{\sigma_h}\right|\right) = K_S(\Delta r,0), \tag{9.13}$$

(and to (9.7) when $\underset{\sim}{\Delta r} \to 0$).

From (9.13) we can obtain the desired wave number spectrum $W_2(\underset{\sim}{k},0)_S$, (2.3). Noting the isotropy of our model (9.13), we have

$$W_2(k,0)_S = \iint_{[\underset{\sim}{\Delta r}]} K_S(\underset{\sim}{\Delta r},0) e^{i\underset{\sim}{k}\cdot\underset{\sim}{\Delta r}}\, d(\underset{\sim}{\Delta r}) \tag{9.14a}$$

$$= 4\pi\sigma_S^2\sigma_h \int_0^\infty J_0(k\Delta r) K_1(2\Delta r/\sigma_h)(\Delta r)^2\, d(\Delta r), \tag{9.14b}$$

which from [30], p. 410, Eq. (2) becomes finally

$$\boxed{W_2(\underset{\sim}{k},0)_S = \frac{\pi\sigma_S^2\sigma_h^2}{[1+(k\sigma_h/2)^2]^2} = W_2(k,0)_S.} \tag{9.15}$$

[In the present application $k = 2k_o \sin\theta_{oT}$, $(\phi_{oT} = \pi/2)$, cf. Sec. 2 and Fig. 2.1.]

Finally, we comment on various assumptions underlying our present model. We note that

(1). The soliton speed, c_s, is treated as essentially constant here for the small layer thickness, h_{eff}, deduced to be O(1-3 mm), cf. Table 3.1, this means that h_{eff} does not change appreciably with sizeable changes in v_o: changes in v_o produce changes in L_o, cf. (9.3), but not in h_{eff}. This latter is consistent with (9.5). Thus, although v_d can have sizeable variances, cf. Sec. (8.1) and Eq. (4.2), the effective layer h_{eff} remains unchanged, once the soliton process has been established. While this appears plausible and gives results quite consistent with the experimental data, the assumption of the constancy of c_s needs to be directly verified.

(2). The soliton field is taken to be (semi-)isotropic, cf. (9.11) et seq., with soliton motion in the direction of "downwind." This semi-isotropicity is probably not often the actual condition: the soliton field is anisotropic, much like that of the gravity-

capillary wave surface. However, we expect that numerical differences are subsumed (i.e., disguised) in the various scaling parameters, σ_h, σ_S, and are not distinguishable at the present level of experimental refinement. Again, these effects need to be isolated in properly controlled experiments.

The detailed structure of the present model continues to be investigated by the author.

From (9.9) and (9.15) we observe the limiting behavior of these spectra as frequency increases. Thus, we have (as f_s and $k \to \infty$):

$$W_s(f_s) \sim 8\pi c_s^2 \left(\frac{\sigma_S}{\sigma_h}\right)^2 \cdot \frac{1}{\omega_s^3} \; ; \quad W_2(k,0)_S \sim 16\pi \left(\frac{\sigma_S}{\sigma_h}\right)^2 \frac{1}{k^4} \; , \tag{9.16}$$

showing the expected k^{-4} and f_s^{-3} structure. Both spectra exhibit this behavior in excellent agreement with experiment ([8], [26] for k^{-4}-dependence, for example, and Fig. 16 of [32], and in [13]; and [14] for f_s^{-3}-dependence). [Of course, ultimately these dependences must fall off faster, in order to ensure the physically required finite rms slopes. This implies a fall-off at least $O(k^{-5}$ or $f_s^{-4})$, or if fractional exponents are allowed, at least as $O(k^{-4-\varepsilon}$ or $f_s^{-3-\varepsilon}$, $\varepsilon > 0)$.]

10. Doppler Spread II: Determination of ΔF

With the results of Secs. (8.1)-(8.3) we are ready to determine the spectral spread, ΔF, whose precise form we define below. To evaluate ΔF we return to (6.3) and insert (8.3), (8.19), (8.29a) as indicated. The result is explicitly,

$$M_{RT}^{(0)}(\tau \mid f_o) = (\overline{R_o^2}\,\overline{S^2}\, k_o^2 g_T g_R \tfrac{A}{2})N_{GS}^{(0)}(\underset{\sim}{\alpha}_{o\perp}) e^{2ik_o \underset{\sim}{\alpha}_{o\perp} \cdot \underset{\sim}{\bar{v}}_{oD}\tau} \cdot e^{-\sigma_\Delta^2 \tau^2/2}$$

$$\cdot \iint_{[\Delta r]} e^{2ik_o \underset{\sim}{\alpha}_{o\perp} \cdot \underset{\sim}{\Delta r}} K_S(\underset{\sim}{\Delta r}, \tau) d(\underset{\sim}{\Delta r}), \tag{10.1}$$

where now

$$\boxed{\sigma_\Delta^2 \equiv \omega_o^2\sigma_\beta^2 + \omega_o^2 R_{\dot{\zeta}} + R_G} \tag{10.2}$$

is the spread-coefficient. Applying (10.1) to (6.2) gives directly the intensity spectrum of the received (incoherent) component of the back-scatter, $X-\langle X\rangle$:

$$W_{X-\langle X\rangle}(f) = 2k_o^2 G^{(1)}{}_B \int_{-\infty}^{\infty} d\tau\, e^{-\sigma_\Delta^2\tau^2/2 - i\omega\tau} \mathrm{Re}\{K_o(\tau)_{in} e^{-i\omega_o\tau + i2k_o \underset{\sim}{\alpha}_{o\perp}\cdot\bar{\underset{\sim}{v}}_o D\tau}$$

$$\cdot \iint_{[\underset{\sim}{\Delta r}]} K_S e^{2ik_o \underset{\sim}{\alpha}_{o\perp}\cdot\underset{\sim}{\Delta r}} d(\underset{\sim}{\Delta r})\ \}\ . \tag{10.3}$$

At this point we use the directional form (7.8) for the soliton surface waves, e.g.,

$$K_S(\underset{\sim}{\Delta r},\tau) = \int_0^\infty W_S(f_s) \langle \cos(\omega_s\tau - \underset{\sim}{K_s}\cdot\underset{\sim}{\Delta r}\rangle_\alpha df_s . \tag{10.4}$$

Inserting (10.4) into the integral over $\underset{\sim}{\Delta r}$ in (10.3), in the manner of (7.9), gives us for these solitons

$$\Phi_S(\underset{\sim}{\nu_o},\tau) = \frac{c_s}{2\nu_o} W_S(c_s\nu_o) w_1(\phi_{\nu_o})_\alpha\, e^{ik_o|2\underset{\sim}{\alpha}_{o\perp}|c_s\tau}\ , \tag{10.5}$$

which reveals the Bragg scatter doppler explicitly. With (10.5) we get for (10.3) at once

$$\boxed{W_{X-\langle X\rangle}(f) = C_o \int_{-\infty}^{\infty} e^{-\sigma_\Delta^2\tau^2 - i\omega\tau} \mathrm{Re}\{K_o(\tau)_{in} e^{-i(\omega_o+\delta\omega_o)\tau}\}d\tau\ ,} \tag{10.6}$$

where the mean doppler shift is, as expected,

$$\delta\omega_o = -[2\underset{\sim}{\alpha}_{o\perp}\cdot\bar{\underset{\sim}{v}}_{oD}/c_o + 2|\underset{\sim}{\alpha}_{o\perp}|c_s/c_o]\omega_o, \tag{10.6a}$$

cf. (7.21), and

$$C_o \equiv 2k_o^2 G(1) B \frac{c_s}{2\nu_o} W_S(c_s\nu_o) w_1(\phi_{\nu_o})_\alpha \; ; \quad B \equiv \overline{R_o^2}\;\overline{S^2}\; k_o^2 g_T g_R \frac{A}{2} N_{GS}^{(0)}(\underset{\sim}{\alpha}_{o\perp}), \tag{10.6b}$$

with

$$\nu_o = 2k_o|\underset{\sim}{\alpha}_{o\perp}|/2\pi = \frac{\omega_o}{\pi c_o}\{\hat{\underset{\sim}{i}}_x \cos\phi_{oT}\sin\theta_{oT} + \hat{\underset{\sim}{i}}_y \sin\phi_{oT}\sin\theta_{oT}\}, \tag{10.6c}$$

cf. (7.7). (An interesting feature to note about our result (10.6) is that the spectral density W_S of the soliton surface appears as a constant factor of the integral, cf. (10.8) ff.)

Observing that $K_o(\tau)_{in}$ is even, cf. (6.2b), and considering only positive frequencies ($f > 0$), we see that (10.6) reduces to

$$\boxed{W_{X-\langle X\rangle}(f) = C_o \int_0^\infty K_o(\tau)_{in} e^{-\sigma_\Delta^2\tau^2/2} \cos[\omega-(\omega_o+\delta\omega_o)]\tau \; d\tau.} \tag{10.7}$$

Equation (10.7) shows the spreading and frequency shift produced in the incident (narrow-band) signal by interaction with the complex wave surface of our model. If long cw pulses are used, i.e., long compared to the decay time $\tau_\Delta = \sigma_\Delta^{-1}$, which is the case here, we can replace $K_o(\tau)_{in}$ by $A_o^2/2$ for an effectively cw signal. Then, (10.7) reduces further to

$$W_{X-\langle X\rangle}(f) = \frac{C_o A_o^2}{2} \int_0^\infty e^{-\sigma_\Delta^2\tau^2/2} \cos(\omega-b_{oc})\tau \; d\tau \tag{10.8a}$$

$$= \frac{C_o A_o^2}{\sigma_\Delta} \sqrt{\frac{\pi}{2}}\, e^{-b_{oc}^2/2\sigma_\Delta^2}. \tag{10.8b}$$

The (two-sided) doppler spectral spread, ΔF, about the doppler shifted carrier, $f_o+\delta f_o$, is defined by

$$\boxed{\Delta F \equiv 2\cdot\frac{\hat{b}_{oc}}{2\pi} = \frac{\hat{b}_{oc}}{\pi}\ ,} \tag{10.9}$$

where the angular frequency $\hat{b}_{oc}$ is that for which the following relation holds:

$$\frac{W_{X-\langle X\rangle}(b_{oc})}{W_{X-\langle X\rangle}(0)} = \frac{1}{\hat{C}}\ ; \quad \hat{C} \equiv 10\ \log_{10}e = 4.34. \tag{10.10}$$

Accordingly, using (10.8b) in (10.10) gives at once

$$\hat{b}_{oc} = \sqrt{2\sigma_\Delta^2\ \log\ \hat{C}} = 1.714\ \sigma_\Delta; \quad (\sqrt{2\ \log\ \hat{C}} = 1.714). \tag{10.11}$$

Finally, putting (10.2) together with (10.9)-(10.11) we obtain the desired expression for the doppler (frequency) spread:

$$\boxed{\Delta F = \frac{1.714}{\pi}\ (2\alpha_{oz}k_o\sigma_{\dot\zeta})\ \sqrt{1 + \frac{\sigma_\beta^2}{(2\alpha_{oz}\sigma_{\dot\zeta}/c_o)^2} + \frac{R_G}{k_o^2(2\alpha_{oz}\sigma_{\dot\zeta})^2}}\ .} \tag{10.12}$$

Given ΔF by experiment at two different frequencies enables us to estimate σ_β^2 and R_G, as we describe in Sec. 4. We note again that to obtain ΔF here it is not necessary to evaluate $K_S(\underset{\sim}{\Delta r},\tau)$ explicitly, or correspondingly, W_S, cf. (10.5). The same is true of the doppler shift δf_o, cf. Sec. 7. Of course, if we wish the spectral density $W_{X-\langle X\rangle}$, or the backscatter cross section (cf. Sec. 2), the structure of $K_S(\underset{\sim}{\Delta r},\tau)$ is required.

References

[1]. D. Middleton, "Acoustic Scattering Cross-Sections for Truly Composite Wind-Wave Surfaces: Scattering without Bubbles," NUSC Tech. Doc. 7205, August 20, 1984, Naval Underwater Systems Center, New London, Conn. 06320.

[2]. W. I. Roderick and J. B. Chester, R. K. Dullea, "High-Frequency Acoustic Backscatter from the Sea Surface," NUSC Tech. Doc. 7183, July 12, 1984, Naval Underwater Systems Center, New London, Conn. 06320.

[3]. D. Middleton, "Soliton Mechanisms in Wind-Wave Surface Scattering, I. Underwater Acoustic Scatter Models," NUSC Tech. Doc., in preparation, Spring, 1986, Naval Underwater Systems Center, New London, Conn. 06320.

[4]. D. Middleton and R. H. Mellen, "Wind-Generated Solitons: A Potentially Significant Mechanism in Ocean Surface Wave Generation and Surface Scattering," Letter to the Editor, IEEE Journal of Oceanic Engineering, Vol. OE-10, No. 4 (Oct.), 1985, pp. 471-476.

[5]. S. T. McDaniel and A. D. Gorman, "Acoustic and Radar Sea-Surface Backscatter," J. Geophysical Research 87, 4127-4136, 1982, and experimental references therein.

[6]. _____, "Examination of the Composite-Roughness Scattering Model," JASA 73, No. 5, May 1983, pp. 1476-1486, and references.

[7]. G. P. deLoor, "Project Noordwijk, Part III: The radar backscatter coefficient (γ) as measured at Platform Noordwijk and comparison with other data," Nat'l. Defense Research Org. TNO, The Netherlands, Rep. PHL 1982-22 May 1982.

[8]. R. T. Lawner and R. K. Moore, "Short Gravity and Capillary Wave Spectra from Tower-Based Radar," IEEE Journal of Oceanic Engineering, Vol. OE-9, pp. 317-324, No. 5, Dec. 1984.

[9]. L. Brekhovskikh and Yu. Lysanov, Fundamentals of Ocean Acoustics (Springer Series in Elecktro-physics 8), Springer-Verlag (New York), 1982. See Sec. 1.6, Fig. 1.26 and remarks; also p. 203 and comments, with Fig. 9.10.

[10]. J. Lighthill, Waves in Fluids, Camb. Univ. Press (New York), 1979 (paperback ed.), pp. 463-468; p. 467.

[11]. R. K. Dodd et al., Solitons and Nonlinear Wave Equations, Academic Press (New York), 1982, 1984 ed., Secs. 1.2, 5.3, for example.

[12]. O. Shemdin, "Wind-generated Current and Phase Speed of Wind Waves," J. of Physical Oceanography, pp. 411-419, Vol. 2, Oct., 1972.

[13]. H. Mitsuyasu and T. Honda, "The High Frequency Spectrum of Wind-Generated Waves," J. of the Oceanographic Soc. of Japan 30, pp. 185-198, 1974.

[14]. H. Mitsuyasu, "Measurement of the High-Frequency Spectrum of Ocean Surface Waves," J. of Physical Oceanography 7, pp. 882-891, Nov. 1977.

[15]. W. L. Pierson, Jr., and L. Moskowitz, "A Proposed Spectral Form for Fully-Developed Wind Seas Based on the Similarity Theory of S. A. Kitaigorodskii," J. Geophysical Research 69, 5180-5190, No. 24, 1964. See also Sec. 6.3 of The Physics of Air-Sea Interaction, S. A. Kitaigorodskii [Transl. 1973, Israel Program for Scientific Translations for U.S. Dept. of Commerce, available NTIS, Springfield, Va. 22151].

[16]. N. N. Galubin, Akus. Zhur. 22, 343-350, 1976. English Transl.: Soviet Physical Acoustics 23, 193-197, (1976); see also Fig. 1.26 of [4] and text.

[17]. C. S. Cox and W. H. Munk, "Measurement of the Roughness of the Sea Surface from Photographs of the Sun's Glitter," J. Optical Soc. Amer. 44, No. 11, pp. 838-850, 1954.

[18]. F. G. Bass and I. M. Fuks, Wave Scattering from Statistically Rough Surfaces, Transl. and Ed. by G. B. Vesecky and J. F. Vesecky, International Series in Natural Philosophy, Vol. 93, 1979, Pergamon Press, New York.

[19]. D. Middleton, "Intermediate and High-Frequency Acoustic Backscattering Cross Sections for Water-Ice Interfaces: I. Two-Component Profile Models," NUSC Tech. Doc. 7375, March 7, 1985, Naval Underwater Systems Center, New London, Conn. 06320.

[20]. M. Olsen, H. Smith, and A. C. Scott, "Solitons in a Wave Tank," Amer. J. of Physics 52, (19), pp. 826-830, Sept., 1984.

[21]. V. P. Glotov, "Low-Frequency Sound Scattering by Wind-Generated Air Bubbles Below a Sea Surface with Large-Scale Roughness," Akus. Zhur. 24, No. (6), 854-860 (Nov./Dec.), 1978. Transl. Sov. Phys. Acoustics, 1979, Amer. Inst. of Physics.

[22]. S. A. Thorpe, "On the Clouds of Bubbles Formed by Breaking Wind Waves in Deep Water and Their Role in Air/Sea Gas Transfer," Phil. Trans. Roy. Soc. (London) A304, pp. 155-210, 1982.

[23]. D. Middleton, "Doppler Effects for Randomly Moving Scatterers and Platforms," JASA 61, No. 5, May, 1977, pp. 1231-1250.

[24]. _____, An Introduction to Statistical Communication Theory, McGraw-Hill (New York), 1960.

[25]. A. Ramamonjiariosa, S. Baldey, and I. Choi, "Laboratory Studies on Wind-Wave Generation, Amplification, and Evolution," in Turbulent Fluxes Through the Sea Surface, Wave Dynamics, and Prediction, Ed. A. Favré and K. Hasselmann, pp. 403-420.

[26]. B. Kinsman, Wind Waves, Prentice-Hall, Englewood Cliffs, N.J., 1965; Section 8.3, cf. Eq. (8.33) et seq.

[27]. L. Fortuin, The Sea Surface as a Random Filter for Underwater Sound Waves, Doctoral Dissert., Twente Tech. Hoch., Delft, The Netherlands, 1973.

[28]. D. Middleton, Research Notes, ONR Contract N00014-81-C-0258 (1981).

[29]. F. G. Bass, I. M. Fuks, A. I. Kalmykov, I. E. Ostrovsky, and A. D. Rosenberg, "Very High Frequency Radiowave Scattering by a Disturbed Sea Surface," IEEE Trans. on Antennas and Propagation, Vol. AP-16, No. 5, September, 1968, pp. 554-568.

[30]. G. N. Watson, Theory of Bessel Functions, McMillan (New York), 1944.

[31]. G. E. Peterson, "Electrical Transmission Lines as Models for Soliton Propagation in Materials: Elementary Aspects of Video Solitons," AT&T Bell Labs. Tech. J., July-Aug., 1984, Vol. 63, No. 6, pp. 901-919. In particular, see Fig. 6 and text p. 913, Sec. 3.3. Note the description of pulses--in our study here, hydraulic shock waves--into ensembles of solitons.

[32]. R. H. Mellen, D. Middleton, and J. W. Fitzgerald, "Sea Surface Backscattering and the Soliton Mechanism, NUSC Technical Doc. 7583, Jan., 1986, Naval Underwater Systems Center, New London, Conn. 06320.

INITIAL DISTRIBUTION LIST

Addressee	No. of Copies
NAVSEASYSCOM, SEA-63D (CDR E. Graham)	1
NORDA, Code 530, 113 (B. Adams, Dr. R. Farwell T. Goldsberry, Dr. M. Y. Su) 240 (W. Kinney)	6
NOSC, Code 013 (Dr. E. Cooper) (3), 7133 (Dr. C. Persons), 5322 (Dr. J. Northrup), (B. Smith), (Dr. F. Fisher, Dr. F. Spiess (Marine Physical Labs))	8
SACLANTCTR (Tech. Director, R. Goodman)	1
ONR, Code 1125UA (Dr. R. M. Fitzgerald, Dr. R. Sternberg), 1125AR (R. Obrochta), 1111SP (Dr. N. Gerr), 111 (Dr. T. Berlincourt), 112 (G. Hamilton), 1122B (E. Hartwig), 1111 (Dr. E. Wegman, Dr. Ringersen)	9
NRL (E. Franchi, Dr. L. Wetzel (Code 5303))	2
ITS/NTIA: U.S Dept. of Commerce (Dr. A. Spaulding, Dr. C. Rush)	20
ARL, UNIV OF TEXAS (Dr. G. Wilson, G. Ellis, Prof. C. Horton, Dr. H. Boheme)	4
DTIC	12
NAVPGSCOL (Prof. H. Medwin, (1) Library)	2
Science Applications Inc. (W. Chadsey, Dr. R. Becherer, Dr. Tatrow, Dr. M. J. Brackett Hersey, Dr. R. Green)	5
YALE UNIVERSITY (Prof. P. H. Schultheiss)	1
Scripps Inst. of Oceanography, La Jolla, CA (Dr. W. Munk)	1
ARL/PENN STATE, STATE COLLEGE, PA (Dr. S. McDaniel, D. McCammon, F. Symon)	4
"Cyberlink," Boulder, CO (Dr. P. McManamon)	1
APL, Johns Hopkins (Dr. J. Apel)	1
WPL-NOAA (Wave Propagation Lab) (Dr. S. Clifford)	1
NOAA, Dir. of NOAA Labs, Dr. V. Derr)	1
Johns Hopkins Univ. Dept. of Oceanography (Prof. O. M. Phillips)	1
UNIV OF WISCONSIN, Dept. of Geophysics (Prof. C. S. Clay)	1
UNIV OF NEW MEXICO, Dept. of Elec. Eng. (Prof. D. Petersen)	1
PSI Inc. (Dr. R. Mellen, J. Fitzgerald)	2
UNIV OF MIAMI/RSMAS (Dr. F. Tappert)	1
Dr. David Middleton, New York, NY	15
APL/UW, (E. Thorsos, D. Jackson, S. McConnell)	3
ONT (T. Warfield, T. Kooij, B. Palmer)	3
NADC, Code 3042 (T. Polaneczky)	1
UNIV OF ILLINOIS (V. Twersky)	1
FWG/Kiel, Germany (G. Ziehm, H. Herwig, B. Nuetzel)	3
UNIV OF KANSAS (Dr. R. T. Lawner, R. K. Moore)	2
SONALYSTS, Inc. (W. Pugliese)	1
UNIV OF WASHINGTON, Dept. of Elec. Eng. and App. Math. (Prof. A. Ishimaru)	1
UNIV OF NEBRASKA, Dept. of Elec. Eng. (Prof. E. Bahar)	1
DARPA (C. Stewart)	1
NCSC (L. J. Satkowiak)	1